SCALABLE HIERARCHICAL PDE SAMPLER FOR GENERATING SPATIALLY CORRELATED RANDOM FIELDS USING NON-MATCHING MESHES [*][†]

SARAH OSBORN [‡], PATRICK ZULIAN[§], THOMAS BENSON [‡], UMBERTO VILLA [¶], ROLF KRAUSE[§], AND PANAYOT S. VASSILEVSKI [‡][‖]

Abstract. This work describes a domain embedding technique between two non-matching meshes used for generating realizations of spatially correlated random fields with applications to large-scale sampling-based uncertainty quantification. The goal is to apply the multilevel Monte Carlo (MLMC) method for the quantification of output uncertainties of PDEs with random input coefficients on general, unstructured computational domains. We propose a highly scalable, hierarchical sampling method to generate realizations of a Gaussian random field on a given unstructured mesh by solving a reaction-diffusion PDE with a stochastic right-hand side. The stochastic PDE is discretized using the mixed finite element method on an embedded domain with a structured mesh, and then the solution is projected onto the unstructured mesh. This work describes implementation details on how to efficiently transfer data from the structured and unstructured meshes at coarse levels, assuming this can be done efficiently on the finest level. We investigate the efficiency and parallel scalability of the technique for the scalable generation of Gaussian random fields in three dimensions. An application of the MLMC method is presented for quantifying uncertainties of subsurface flow problems. We demonstrate the scalability of the sampling method with non-matching mesh embedding, coupled with a parallel forward model problem solver, for large-scale 3D MLMC simulations with up to $1.9 \cdot 10^9$ unknowns.

Key words. multilevel methods; PDEs with random input data; PDE sampler; non-matching meshes; H(div) problems; mixed finite elements; uncertainty quantification; multilevel Monte Carlo

1. Introduction. Many mathematical models of physical phenomena involve spatially varying input data which is often subject to uncertainty. This uncertainty will propagate through a simulation and lead to uncertainty in the output. The goal in forward propagation of uncertainty is to quantify the effect of the input uncertainties in the output of numerical simulations. We consider models based on partial differential equations (PDEs) with spatially correlated input coefficients subject to uncertainty that are modeled as a random field with particular statistical properties. Then our goal is to compute statistics of the solution to the PDE with random input coefficients for large-scale problems using Monte Carlo methods. In particular, we consider the multilevel Monte Carlo (MLMC) method, which runs repeated simulations at random realizations of the uncertain input data on a hierarchy of spatial resolutions. Then, the approximations are used to compute corresponding sample averages of the desired statistics of the solution of the PDE.

As an example model problem, we consider the simulation of subsurface flows governed by Darcy's law. The permeability tensor, k, is often subject to uncertainty, due to a lack of knowledge of the porous medium at all locations. To account for this uncertainty, the permeability field is modeled as a random field with given mean and covariance structure. Estimating the impact of uncertainty on the results of a

groundwater flow simulation is useful in many situations, for example in risk analysis for radioactive waste disposal or in oil reservoir simulations.

Monte Carlo techniques are a widely used class of methods to estimate particular quantities of interest for PDEs with random input coefficients, and require the solution of the model problem equations for many different realizations of k. The computational cost for large-scale problems can often be prohibitively large, as computing each sample amounts to solving a PDE with a fine mesh. MLMC methods [1, 2] are used to accelerate the convergence of standard Monte Carlo methods and offer significant computational savings. These methods employ a hierarchy of spatial resolutions as a variance reduction technique for the approximation of expected quantities of interest and have been successfully applied to a wide variety of applications; see, e.g., [3, 4, 5, 6, 7]. As in [8], for our MLMC simulations we consider a general unstructured fine grid and construct a hierarchy of algebraically coarsened grids and finite element spaces using element-based algebraic multigrid techniques (AMGe), which possess the same order approximation property as the original fine level discretization, see e.g., [9, 10, 11]. Of particular importance is the ability to run MLMC simulations on large-scale unstructured meshes of complicated computational domains. To accomplish this task, input realizations of the random field must first be generated for general unstructured meshes. Thus, an important task for large-scale MLMC simulations is the scalable generation of Gaussian random field realizations, which is the focus of this work.

A common choice in stochastic modeling for subsurface hydrology is to model the random permeability, k, as a log-normal random field, so that $k(\mathbf{x}, \omega) = \exp[\theta(\mathbf{x}, \omega)]$, where $\theta(\mathbf{x}, \omega)$ is a Gaussian random field with prescribed mean and covariance structure; see, e.g., [12, 13]. Several methods exist to realize samples of Gaussian random fields to be used in MLMC simulations. The widely-used Karhunen-Loève (KL) expansion [14] provides an infinite series representation of the random field involving the eigenvalues and eigenvectors of the integral operator associated with the covariance function. In practical computations, the series is truncated, which results in a truncation error (bias) in a Monte Carlo simulation. Additionally, the computation quickly becomes infeasible for large-scale simulations as a dense eigenvalue problem must be solved. Approaches based on randomized methods and hierarchical semi-separable matrices can drastically reduce the cost of solving the eigenvalue problem (see, e.g., [15]); however, only the dominant eigenmodes of the KL expansion are computed and, therefore, introduce bias in the sampling. Circulant embedding [16, 17] offers a fast and exact simulation of stationary Gaussian random fields on a regular grid. This method exploits the Fast Fourier Transform (FFT) method to implicitly construct a basis that (block)-diagonalizes the covariance matrix. However, the computational cost of the method depends on the correlation length of the random field. Additionally, the random field is assumed to be stationary, whereas our proposed method can handle correlation functions and marginal variance functions that are space-dependent. Last but not least, although scalable implementations of three-dimensional FFT are available (see, e.g. [18, 19]), we are not aware of any parallel publicly available implementations of circulant embedding for large-scale computations. For these reasons, we do not pursue this approach.

An alternative technique for generating realizations of $\theta(\mathbf{x}, \omega)$ relies on the link between Gaussian fields and Gaussian Markov random fields, where a stochastic partial differential equation (SPDE) with a white noise forcing term is solved to generate the desired realizations [20, 21, 22]. This approach provides a sampling method that is highly scalable as the method leverages solution strategies for solving sparse linear

systems arising from the finite element discretization of the SPDE, as investigated in [8]. A limitation of the SPDE sampling method is that the computed realizations contain artificial boundary effects, arising from the discretization of the SPDE on a finite domain. A possible solution is to embed the computational domain into a larger one as investigated in [8]; however, this poses some challenges for unstructured meshes.

As a follow-up and as an alternative to the method proposed in [8], we propose a scalable domain embedding technique using non-matching meshes. The SPDE with white noise forcing term is discretized and solved on a regular, structured mesh, then is projected back to the original, unstructured mesh of interest. We use a completely parallel approach that allows for the transfer of discrete fields between unstructured volume and surface meshes, which can be arbitrarily distributed among different processors [23]. Then the resulting realization of the random field can be used as the input realization of a Monte Carlo method.

The key contribution of this work is to provide a flexible, black-box workflow for embedding complex 3D domains in parallel for a highly scalable, hierarchical sampler of Gaussian random fields. The domain embedding is necessary for the alleviation of boundary artifacts in the SPDE sampler, and allows for the use of more efficient solvers for structured grids. In particular, we will use a scalable hybridization multigrid preconditioning strategy. This sampling technique allows for the use of unstructured meshes for complex computational geometries in 3D, which is necessary for realistic subsurface flow simulations.

The focus of this work is on making MLMC simulations feasible in practice for large-scale problems. To this end, we focus on parallelism across the spatial domain in computing realizations of the input random field using a novel technique, then performing the subsequent solve of the model of interest in parallel. Using the presented sampling strategy, coupled with scalable techniques for the solution of the forward model problem, we demonstrate that the approach allows for the solution of an extreme-scale forward UQ problem with $1.9 \cdot 10^9$ unknowns with high accuracy. Moreover, scalability of our approach can be further improved by exploiting additional levels of parallelism, such as the scheduling approach [24], where the authors investigate the complex task of scheduling parallel tasks within and across levels of MLMC.

The remainder of the paper is organized as follows. The standard Monte Carlo and MLMC methods are reviewed in Section 2. The forward model problem and discretization is described in Section 3. In Section 4 we discuss a method for generating realizations of spatially correlated random fields based on Gaussian Markov random fields. The sampling method is based on solving a mixed discretization of a reaction-diffusion equation with a stochastic right-hand side using domain embedding with two non-matching meshes. The scalable mapping of discrete fields between non-matching meshes is discussed, and a brief overview of the implementation details of the projection operator is provided in Section 5. The hierarchical SPDE sampling procedure is introduced and examined in Section 6. Additionally, we discuss the iterative solution strategy solving for the resulting saddle-point mixed systems. Numerical results are presented in Section 7 that investigate the parallel performance of the proposed sampling method, and an adaptive MLMC simulation for uncertainty quantification in subsurface flow using different geometries in three spatial dimensions. Concluding remarks are given in Section 8.

2. Multilevel Monte Carlo Methods. In this section we briefly review the standard Monte Carlo (MC) method and the MLMC method for computing moments of quantities of interest $Q(\omega) = \mathcal{B}[\mathbf{X}(\mathbf{x}, \omega)]$, where $\mathbf{X}(\mathbf{x}, \omega)$ is the solution of a PDE with random input coefficient following the presentation in [4]. In our model problem, the quantity of interest is related to the pressure and/or Darcy flux of the mixed Darcy equations (3.1). In practice, the inaccessible quantity of interest $Q(\omega)$ is approximated by $Q_h(\omega)$, the functional of the finite element solution $\mathbf{X_h}(\mathbf{x}, \omega)$ on the triangulation $\mathcal{T}_h$.

2.1. Standard Monte Carlo simulation. The standard Monte Carlo estimator for $\mathbb{E}[Q]$ is

$$(2.1) \qquad \widehat{Q}_h^{MC} = \frac{1}{N} \sum_{i=1}^{N} Q_h^i,$$

where Q_h^i is the ith sample of Q_h and N is the number of (independent) samples.

The mean square error (MSE) of the method is given by

$$(2.2) \qquad \mathbb{E}\left[(\widehat{Q}_h^{MC} - \mathbb{E}[Q])^2\right] = \frac{1}{N} \mathbb{V}[Q_h] + (\mathbb{E}[Q_h - Q])^2.$$

Thus, the error naturally splits into two terms: the sampling error given by the variance of the estimator, and the estimator bias related to the finite element discretization error. The estimator variance decays linearly with respect to the sample size N, and the bias gets smaller as the discretization is refined. This can make the method prohibitively expensive as the necessary samples size becomes very large and a fine spatial discretization is necessary for high accuracy.

2.2. Multilevel Monte Carlo simulation. The MLMC method [4, 2] is an effective variance reduction technique, which reduces the overall computational cost of the standard MC method using a hierarchical sampling technique. Assume we have a sequence $Q_L, \ldots, Q_1$ which approximates the quantity of interest $Q_0 = Q_h$ with increasing accuracy and increasing cost. The sequence of approximations is often found by solving the model problem on a geometric hierarchy of meshes constructed by uniform refinement, but other alternative options have been considered; see, e.g., [25]. As in [8], we consider a nested hierarchy of spatial approximations constructed from AMGe methods for finite element discretizations, which possess the same order approximation property as the original fine level discretization, discussed in Section 3.1.

Using the linearity of the expectation operator, we have the following expression for $\mathbb{E}[Q_h]$ based on corrections with respect to the next coarser discretization level:

$$(2.3) \qquad \mathbb{E}[Q_h] = \mathbb{E}[Q_L] + \sum_{\ell=0}^{L-1} \mathbb{E}[Q_\ell - Q_{\ell+1}] = \sum_{\ell=0}^{L} \mathbb{E}[Y_\ell],$$

where $Y_\ell := Q_\ell - Q_{\ell+1}$ for $i = 0, \ldots L - 1$ and $Y_L := Q_L$. A standard MC estimator is used to independently estimate the expectation of Y_ℓ on each level, with suitably chosen samples sizes to minimize the overall computational complexity, yielding the MLMC estimator for (2.3) given by

$$(2.4) \qquad \widehat{Q}_h^{MLMC} = \sum_{\ell=0}^{L} \left[\frac{1}{N_\ell} \sum_{i=1}^{N_\ell} Y_\ell^{(i)} \right].$$

It is important to note that in (2.4) for a particular level ℓ, the same random sample $\omega^{(i)}$ is used with two spatial discretizations to compute $\mathbf{X}_\ell(\mathbf{x}, \omega^i)$ and $\mathbf{X}_{\ell+1}(\mathbf{x}, \omega^i)$ when estimating the quantity $Y_\ell^{(i)}$.

The mean square error for the MLMC method becomes

$$(2.5) \qquad \mathbb{E}\left[\left(\widehat{Q}_h^{MLMC} - \mathbb{E}[Q]\right)^2\right] = \sum_{\ell=0}^{L} \frac{1}{N_\ell} \mathbb{V}[Y_\ell] + \left(\mathbb{E}\left[Q_0 - Q\right]\right)^2 .$$

Similar to the standard MC error, the two terms of the MLMC MSE represent the variance of the estimator and the discretization error.

For a prescribed MSE of less than ε^2, the spatial discretization of the finest level of the hierarchy is chosen so the bias term is less than $\varepsilon^2/2$. Then the number of samples at each level ℓ is chosen to minimize the overall computational cost leading to the following formula for the optimal number of samples of each level:

$$(2.6) \qquad N_\ell \propto \sqrt{\frac{\mathbb{V}[Y_\ell]}{C_\ell}} \quad \ell = 0, \ldots, L,$$

where C_ℓ is the cost of computing one sample at level ℓ. We refer to [4, 26] for additional details.

The key idea that leads to computational savings is that fewer samples are necessary to estimate $\mathbb{E}[Y_\ell]$ on finer levels, because $\mathbb{V}[Y_\ell] \to 0$ as $h_\ell \to 0$ as long as Q_h converges to Q in expectation. The number of samples needed on coarser levels is still large, however samples are less expensive to compute. This balancing of errors across the levels of the hierarchy leads to significant improvements in computational time, while maintaining a desired level of accuracy of the estimate.

3. Forward model problem. We are interested in the simulation of steady state groundwater flow, governed by Darcy's law, in a porous medium where the permeability is not fully known. We consider the mixed Darcy equations given by

$$(3.1) \qquad \begin{array}{ll} \frac{1}{k(\mathbf{x}, \omega)} \mathbf{q}(\mathbf{x}, \omega) + \nabla p(\mathbf{x}, \omega) = 0 & \text{in } D, \\ \nabla \cdot \mathbf{q}(\mathbf{x}, \omega) = 0 & \text{in } D, \end{array}$$

with homogeneous Neumann boundary conditions $\mathbf{q} \cdot \mathbf{n} = 0$ on Γ_N and Dirichlet boundary conditions $p = p_D$ on Γ_D. Here, $\Gamma_N \in \partial D$ and $\Gamma_D \in \partial D$ are non overlapping partitions of ∂D, and $\mathbf{n}$ denotes the unit normal vector to ∂D. The uncertain permeability field $k(\mathbf{x}, \omega)$ is modeled as a log-normal random field such that $\log[k(\mathbf{x}, \omega)]$ has a covariance function belonging to the Matérn family, so that the pressure p and Darcy flux $\mathbf{q}$ are random fields as well.

We consider the discretization of (3.1) with a log-normal permeability field using the mixed finite element method [27, 28]; this particular problem formulation has been analyzed in [29]. Assuming we are given an unstructured mesh $\mathcal{T}_h$ exactly covering D, we consider solutions of the Darcy flux $\mathbf{q}_h$ in the the lowest order Raviart–Thomas finite element space denoted by $\mathbf{R}_h \subset \mathbf{R} := H(\text{div}, D)$, and the pressure p_h in the finite element space of piecewise constant function denoted by $\Theta_h \subset \Theta := L^2(D)$. Given an input realization $k_h(\mathbf{x}, \omega)$ as discussed in Section 4, the resulting discretized saddle-point problem can be written as

$$(3.2) \qquad \Lambda(k)_h \mathbf{X}_h := \begin{bmatrix} M(k)_h & B_h^T \\ B_h & 0 \end{bmatrix} \begin{bmatrix} \mathbf{q}_h \\ \mathbf{p}_h \end{bmatrix} = \begin{bmatrix} \mathbf{f}_h \\ 0 \end{bmatrix} := \mathbf{G}_h,$$

where $\mathbf{f}_h$ stems from the discretization of the Dirichlet boundary condition $p = p_D$ on Γ_D.

3.1. Multilevel formulation. We now consider the discretization of (3.1) on a hierarchy of levels, as needed by the MLMC algorithm. Given the unstructured mesh $\mathcal{T}_h$ of D, we assume that a sequence of unstructured meshes $\mathcal{T}_\ell$ for $\ell = 1, \ldots, L$ on D has been generated by recursively agglomerating finer level elements. We denote the finest level mesh $\mathcal{T}_h$ as $\mathcal{T}_0$, whereas $\mathcal{T}_L$ corresponds to the coarsest level. For each coarse level, we construct the corresponding finite element spaces $\mathbf{R}_\ell$, Θ_ℓ, associated with the (agglomerated) mesh $\mathcal{T}_\ell$ using methodology from AMGe methods, so that we are able to construct operator-dependent coarse spaces for $H(\mathrm{div})$ problems with guaranteed approximation properties on general, unstructured grids; see [9, 10, 11, 30] for further details.

We denote the piecewise constant interpolation operators from coarser space $\Theta_{\ell+1}$ to the finer space Θ_ℓ as P_θ for $\ell = 0, \ldots, L-1$. We also define the operators from the coarser space $\mathbf{R}_{\ell+1}$ to the finer space $\mathbf{R}_\ell$ as $P_\mathbf{u}$. These operators are constructed using techniques from AMGe; see [9, 10, 11] for details about the operators P_θ and $P_\mathbf{u}$.

The discrete saddle-point block matrices are labeled $\Lambda(k)_\ell$, corresponding to the pair of finite element spaces $\mathbf{R}_\ell$, Θ_ℓ for $\ell = 0, \ldots, L$. Then, the discrete saddle-point problem (3.2) at coarse level $\ell = 1, \ldots, L$ reads

$$(3.3) \qquad \Lambda(k)_\ell \mathbf{X}_\ell := \begin{bmatrix} M(k)_\ell & B_\ell^T \\ B_\ell & 0 \end{bmatrix} \begin{bmatrix} \mathbf{q}_\ell \\ \mathbf{p}_\ell \end{bmatrix} = \begin{bmatrix} \mathbf{f}_\ell \\ 0 \end{bmatrix} := \mathbf{G}_\ell,$$

where

$$(3.4) \qquad M(k)_\ell := P_\mathbf{u}^T M(k)_{\ell-1} P_\mathbf{u}, \quad B_\ell := P_\theta^T B_{\ell-1} P_\mathbf{u}, \quad \mathbf{f}_\ell := P_\mathbf{u}^T \mathbf{f}_{\ell-1}$$

are the Galerkin projection at level $l = 1, \ldots, L$ of the corresponding fine grid matrices and vectors.

For an efficient MLMC simulation, it is necessary to repeatedly assemble and solve (3.3) on coarse levels $\ell = 1, \ldots, L$ for various realizations of $k_\ell(\mathbf{x}, \omega^{(i)})$ *without visiting the fine grid.*

Since B_ℓ and $\mathbf{G}_\ell$ are independent of $k_\ell(\mathbf{x}, \omega^{(i)})$, such matrices and vectors can be computed once — using the Galerkin projection in (3.4) — before the MLMC simulation. However, the efficient computation of $M(k)_\ell$ on coarse levels requires particular care, since this matrix depends on the random parameter $k_\ell(\mathbf{x}, \omega^{(i)})$. To this aim, we exploit the sophisticated data structures of the AMGe hierarchies, which closely mimic the same data structures of geometric multigrid and include topological tables (i.e., element-element, element-face connectivity) and degree-of-freedom to element mapping for all levels of the hierarchy. Specifically, at each level ℓ we denote with $L_{e_\ell}^{\mathbf{R}_\ell}$ the mapping between local (to the element $e_\ell \in \mathcal{T}_\ell$) and global (for the space $\mathbf{R}_\ell$) degrees of freedom. These local to global mappings are then used to assemble local (to each agglomerated element $e_\ell \in \mathcal{T}_\ell$) mass matrices into the global one. Then, given the piecewise-constant on the elements of $\mathcal{T}_\ell$ input k_ℓ, the global weighted mass matrix $M(k)_\ell$ for the space $\mathbf{R}_\ell$ is computed as

$$(3.5) \qquad M(k)_\ell = \sum_{e_\ell \in \mathcal{T}_\ell} s_{e_\ell} (L_{e_\ell}^{\mathbf{R}_\ell})^T M_{e_\ell} (L_{e_\ell}^{\mathbf{R}_\ell}),$$

where $s_{e_\ell} = k_\ell^{-1}\big|_{e_\ell}$ is the restriction of k_ℓ^{-1} to the element $e_\ell \in \mathcal{T}_\ell$, and $\{M_{e_\ell}\}_{e_\ell \in \mathcal{T}_\ell}$ are the local mass matrices for the space $\mathbf{R}_\ell$. These local matrices are computed

once during the construction of the AMGe hierarchy by local (to each agglomerated element) Galerkin projection of partially assembled mass matrices from the previous (finer) level, and then stored for future use in the MLMC simulation. For details on the assembly procedure see [31, 32], where a time-dependent two-phase porous media flow is solved with optimal complexity on coarse (upscaled) levels, and [33], where a nonlinear scalable multilevel solver for single-phase porous media flow is presented.

3.2. Linear solution of forward model problem. The linear system (3.3) on each level is iteratively solved using preconditioned GMRES. We consider a preconditioner based on the approximate block-LDU factorization of the operator $\Lambda(k)_\ell$, given by:

$$(3.6) \qquad \mathcal{M}(k)_\ell = \begin{bmatrix} I & \\ B_\ell \tilde{M}(k)_\ell^{-1} & I \end{bmatrix} \begin{bmatrix} \tilde{M}(k)_\ell & \\ & -\tilde{S}_\ell \end{bmatrix} \begin{bmatrix} I & \tilde{M}(k)_\ell^{-1} B_\ell^T \\ & I \end{bmatrix}.$$

Here, $\tilde{M}(k)_\ell$ is a *cheap* preconditioner for the mass matrix, $M(k)_\ell$, such as a diagonal approximation or a small number of Gauss-Seidel iterations. We use three Gauss-Seidel iterations in our numerical experiments. $\tilde{S}_\ell = B_\ell \operatorname{diag}(M(k)_\ell)^{-1} B_\ell^T$ is the approximate Schur-complement, which is symmetric positive definite and sparse. In our numerical experiments, we approximate the action of the approximate Schur-complement inverse by a single algebraic multigrid V-cycle; specifically, we use Boomer-AMG from the solvers library *hypre* [34].

REMARK. *It is worth noticing that the dominant cost in applying the preconditioner (3.6) is to approximate the action of $\tilde{S}_\ell^{-1}$. This justifies the use of a full LDU factorization instead of simpler methods, such as block-diagonal or even block-triangular approaches [35]. Our numerical studies showed that the performance of the full LDU approach was better not only in terms of number of iterations, but also in total solve time compared to the other methods.*

4. Gaussian Markov random field based sampling techniques for spatially correlated random fields. In this section we discuss generating realizations of a log-normal random field, $k(\mathbf{x}, \omega) = \exp[\theta(\mathbf{x}, \omega)]$, where $\theta(\mathbf{x}, \omega)$ is a Gaussian random field with a certain mean and covariance structure to be used as input coefficients for a MLMC simulation. We extend the sampling strategy of [8] to include a scalable domain embedding technique allowing the use of non-matching meshes to sample from the Gaussian random field $\theta(\mathbf{x}, \omega)$.

In particular, we consider the Matérn family of covariance functions, which is a common choice in geostatistics [36]. The Matérn covariance function is given by

$$(4.1) \qquad \operatorname{cov}(\mathbf{x}, \mathbf{y}) = \frac{\sigma^2}{2^{\nu-1}\Gamma(\nu)} (\kappa \|\mathbf{y} - \mathbf{x}\|)^\nu K_\nu(\kappa \|\mathbf{y} - \mathbf{x}\|),$$

where σ^2 is the marginal variance, $\nu > 0$ determines the mean-square differentiability of the underlying process, $\kappa > 0$ is a scaling factor inversely proportional to the correlation length, $\Gamma(\nu)$ is the gamma function, and K_ν is the modified Bessel function of the second kind [37].

To realize a sample of a Gaussian random field with Matérn covariance as in [8], we employ a sampling method that uses a link between Gaussian fields and Gaussian Markov random fields established in [22]. The method utilizes the fact that the solution, $\theta(\mathbf{x}, \omega)$, of the fractional SPDE given by

$$(4.2) \quad (\kappa^2 - \Delta)^{\alpha/2}\theta(\mathbf{x}, \omega) = g\mathcal{W}(\mathbf{x}, \omega) \quad \mathbf{x} \in \mathbb{R}^d (d = 2 \text{ or } 3), \ \alpha = \nu + \frac{d}{2}, \ \kappa > 0, \nu > 0,$$

is a Gaussian field with underlying Matérn covariance [20, 21]. Above, $\mathcal{W}$ is Gaussian white noise, and the scaling factor g is chosen to impose unit marginal variance of the random field as

$$g = (4\pi)^{d/4} \kappa^\nu \sqrt{\frac{\Gamma(\nu + d/2)}{\Gamma(\nu)}}.$$

We restrict the smoothness parameter, ν, to be of the form $\nu = \alpha - d/2$ for an even integer α. Specifically, in three dimensions, the choice of $\nu = 1/2$ results in the random field $\theta(\mathbf{x}, \omega)$ having an underlying exponential covariance structure, as (4.1) reduces to $\mathrm{cov}(\mathbf{x}, \mathbf{y}) = \sigma^2 e^{-\kappa\|\mathbf{y}-\mathbf{x}\|}$.

Then, (4.2) reduces to the following standard reaction-diffusion equation:

$$(4.3) \qquad (\kappa^2 - \Delta)\theta(\mathbf{x}, \omega) = g\mathcal{W}(\mathbf{x}, \omega) \quad \mathbf{x} \in \mathbb{R}^d, \kappa > 0.$$

Thus a scalable sampling method is equivalent to efficiently solving the stochastic reaction-diffusion equation given by (4.3).

It should be noted that defining covariance operators as fractional inverse powers of differential operators is a common approach for the solution of large-scale Bayesian inverse problems governed by PDE forward models, see e.g., [38, 39], as it allows for efficient evaluation of the covariance operator using a fast and scalable multigrid solver. For further details on the approximation of Gaussian random fields with Matérn covariance functions using the Gaussian Markov random field representation of a SPDE, we refer to [22, 40, 41].

4.1. Stochastic PDE sampler. We consider the solution of the stochastic reaction-diffusion equation given by (4.3) to produce realizations of a Gaussian random field using the mixed finite element method on a bounded domain $D \subset \mathbb{R}^d$. When posing the SPDE on a bounded domain, boundary conditions must be imposed, however the proper boundary conditions for the stochastic fields are an open research problem; see, e.g., [42]. We consider using deterministic homogeneous Neumann boundary conditions (zero normal-derivatives); however, this choice introduces boundary artifacts that inflate the variance along the boundary of the domain, as observed in [22].

One approach to mitigate this issue is to extend the domain of interest by a distance greater than the correlation length, solve (4.3) on the extended domain, then restrict the solution back to the original domain to generate a Gaussian field realization. This procedure was explored in [8], and mitigates the artificially inflated variance as the boundary effects are negligible at a distance greater than the correlation length away from the boundary [41]. However, this can pose a challenge with complicated domains and/or unstructured meshes. In this work, we propose an alternative domain embedding technique with two non-matching meshes, using a scalable transfer of discrete fields between the two meshes which can be arbitrarily distributed among different processors, see Section 5. First the SPDE is discretized using the mixed finite element method on an extended regular domain, then the finite element solution is transferred to the original domain resulting in a realization of the Gaussian random field for use as the input coefficient in a Monte Carlo simulation.

4.2. Mixed finite element discretization. Let D be a given polygonal/polyhedral domain with an unstructured mesh $\mathcal{T}_h$. We embed D in an extended regular domain (e.g., a box) $\overline{D}$ meshed by $\overline{\mathcal{T}}_{\bar{h}}$, where $\bar{h} \simeq h$. In contrast to the approach taken in

[8], the two meshes here do not necessarily match on D; in addition, $\overline{\mathcal{T}}_{\bar{h}}$ does not necessarily respect ∂D. We assume that $\overline{\mathcal{T}}_{\bar{h}}$ is obtained by several steps of refinement of an initial coarse mesh. We consider the mixed finite element discretization [27, 28] of (4.3) on the regular domain $\overline{D}$ with mesh $\overline{\mathcal{T}}_{\bar{h}}$. We introduce the functional spaces $\overline{\mathbf{R}} := H(\mathrm{div}, \overline{D})$ and $\overline{\Theta} := L^2(\overline{D})$, as well as the bilinear forms

$$
\begin{aligned}
m(\overline{\mathbf{u}}, \overline{\mathbf{v}}) &:= (\overline{\mathbf{u}}, \overline{\mathbf{v}}) & \forall \overline{\mathbf{u}}, \overline{\mathbf{v}} \in \overline{\mathbf{R}}, \\
w(\overline{\theta}, \overline{q}) &:= (\overline{\theta}, \overline{q}) & \forall \overline{\theta}, \overline{q} \in \overline{\Theta}, \\
b(\overline{\mathbf{u}}, \overline{q}) &:= (\mathrm{div}\, \overline{\mathbf{u}}, \overline{q}) & \forall \overline{\mathbf{u}} \in \overline{\mathbf{R}}, \overline{q} \in \overline{\Theta},
\end{aligned}
$$

and the linear form

$$
\overline{F}^{\mathcal{W}}(\overline{q}) := (\mathcal{W}, \overline{q}) \quad \forall \overline{q} \in \overline{\Theta}.
$$

Above the symbol $(\cdot, \cdot)$ denotes the usual inner product between scalar (vectorial) functions in $L^2(D)$ ($[L^2(D)]^d$).

Let $\overline{\mathbf{R}}_{\bar{h}} \subset \overline{\mathbf{R}}$ denote the lowest order Raviart–Thomas space and $\overline{\Theta}_{\bar{h}} \subset \overline{\Theta}$ denote the finite element space of piecewise constant functions defined on the fine triangulation $\overline{\mathcal{T}}_{\bar{h}}$ of $\overline{D}$, then we seek the solution of the mixed finite element discretization given by

PROBLEM 4.1. *Find $\overline{\mathbf{u}}_{\bar{h}} \in \overline{\mathbf{R}}_{\bar{h}}$ and $\overline{\theta}_{\bar{h}} \in \overline{\Theta}_{\bar{h}}$ such that*

(4.4)
$$
\begin{aligned}
m(\overline{\mathbf{u}}_{\bar{h}}, \, \overline{\mathbf{v}}_{\bar{h}}) + b(\overline{\mathbf{v}}_{\bar{h}}, \, \overline{\theta}_{\bar{h}}) &= 0 & \text{for all } \overline{\mathbf{v}}_{\bar{h}} \in \overline{\mathbf{R}}_{\bar{h}}, \\
b(\overline{\mathbf{u}}_{\bar{h}}, \, \overline{q}_{\bar{h}}) - \kappa^2\, w(\overline{\theta}_{\bar{h}}, \, \overline{q}_{\bar{h}}) &= -g\overline{F}^{\mathcal{W}}(\overline{q}_{\bar{h}}) & \text{for all } \overline{q}_{\bar{h}} \in \overline{\Theta}_{\bar{h}}
\end{aligned}
$$

with essential boundary conditions $\overline{\mathbf{u}}_{\bar{h}} \cdot \mathbf{n} = 0$ on $\partial \overline{D}$.

To formulate the linear algebra representation of the stochastic right hand side $\overline{F}^{\mathcal{W}}(\overline{q}_{\bar{h}})$, two properties of Gaussian white noise defined on a domain $\overline{D}$ are used.

For any set of test functions $\{\overline{q}_i \in L^2(\overline{D}), i = 1, \ldots, n\}$, the expectation and covariance measures are given by

(4.5)
$$
\mathbb{E}[(\overline{q}_i, \mathcal{W})] = 0,
$$

(4.6)
$$
\mathrm{cov}\left((\overline{q}_i, \mathcal{W}), (\overline{q}_j, \mathcal{W})\right) = (\overline{q}_i, \overline{q}_j).
$$

By taking $\overline{q}_i, \overline{q}_j$ as piecewise constants so that $\overline{q}_i, \overline{q}_j \in \overline{\Theta}_{\bar{h}}$, the second equation implies that the covariance measure over a region of the domain is equal to the volume of that region [22]. Then the discrete stochastic linear right hand side is given by

$$
\overline{f}_{\bar{h}} = \overline{W}_{\bar{h}}^{\frac{1}{2}} \xi_{\bar{h}}(\omega), \quad \xi_{\bar{h}}(\omega) \sim \mathcal{N}(0, I)
$$

where $\overline{W}_{\bar{h}}$ is the mass matrix for the space $\overline{\Theta}_{\bar{h}}$, and $\mathcal{N}(0, I)$ denotes the multivariate normal distribution with zero mean and covariance matrix I, that is, each component of $\xi_{\bar{h}}(\omega)$ is standard normal and the components are independent. It should be noted that the mass matrix $\overline{W}_{\bar{h}}$ for the space $\overline{\Theta}_{\bar{h}}$ is diagonal, hence its square root can be computed cheaply.

Then the discrete mixed finite element problem can be written as the linear system

(4.7)
$$
\overline{\mathcal{A}}_{\bar{h}} \overline{U}_{\bar{h}} = \overline{F}_{\bar{h}},
$$

with block matrix and block vectors defined as

(4.8)
$$
\overline{\mathcal{A}}_{\bar{h}} = \begin{bmatrix} \overline{M}_{\bar{h}} & \overline{B}_{\bar{h}}^T \\ \overline{B}_{\bar{h}} & -\kappa^2 \overline{W}_{\bar{h}} \end{bmatrix}, \quad \overline{U}_{\bar{h}} = \begin{bmatrix} \overline{\mathbf{u}}_{\bar{h}} \\ \boldsymbol{\theta}_{\bar{h}} \end{bmatrix}, \quad \overline{F}_{\bar{h}} = \begin{bmatrix} 0 \\ -g\overline{f}_{\bar{h}}(\omega) \end{bmatrix},
$$

where $\overline{f}_{\bar{h}}(\omega) \sim \mathcal{N}(0, \overline{W}_{\bar{h}})$, $\overline{M}_{\bar{h}}$ is the mass matrix for the space $\overline{\mathbf{R}}_{\bar{h}}$, $\overline{B}_{\bar{h}}$ stems from the discretization of the divergence operator, $\overline{W}_{\bar{h}}$ is the (diagonal) mass matrix for the space $\overline{\Theta}_{\bar{h}}$, and $\overline{\mathbf{u}}_{\bar{h}}$, $\overline{\boldsymbol{\theta}}_{\bar{h}}$ are the coefficient vectors of the finite element functions when expanded in terms of the respective basis functions. We remark that the covariance structure of the samples generated by solving the mixed form (4.3) is equivalent to the covariance structure of samples obtained by solving the primal form of the SPDE in [22], as shown in [8]. In fact, using simple algebraic manipulation, it is immediate to show that $\overline{\boldsymbol{\theta}}_{\bar{h}} \sim \mathcal{N}(0, \overline{C}_{\bar{h}})$, where $\overline{C}_{\bar{h}} = \overline{S}_{\bar{h}}^{-1} \overline{W}_{\bar{h}} \overline{S}_{\bar{h}}^{-T}$ and $\overline{S}_{\bar{h}} = \kappa^2 \overline{W}_{\bar{h}} + \overline{B}_{\bar{h}} \overline{M}_{\bar{h}}^{-1} \overline{B}_{\bar{h}}^T$ stems from a nonlocal *discontinuous* Galerkin (interior penalty) discretization of the original PDE (4.3); cf. [43].

5. L^2-Projection. This section concerns a parallel scalable L^2-projection of discrete fields between non-matching partially overlapping meshes. Specifically, in the MLMC simulation we use the L^2-projection to transfer a realization of a Gaussian random field $\overline{\theta}_{\bar{h}}$ on $\overline{\mathcal{T}}_{\bar{h}}$ — computed by solving (4.7) approximately by an iterative method — to the unstructured mesh $\mathcal{T}_h$ of the original domain D, where we then solve the forward problem (3.2).

5.1. Projection between non-matching meshes. Let $\Theta_h = \text{span} \{\varphi_\tau\}_{\tau \in \mathcal{T}_h}$ and $\overline{\Theta}_{\bar{h}} = \text{span} \{\overline{\varphi}_{\overline{\tau}}\}_{\overline{\tau} \in \overline{\mathcal{T}}_{\bar{h}}}$, and assume we have the functions $s \in \Theta_h$ and $\overline{s} \in \overline{\Theta}_{\bar{h}}$. Writing the functions in terms of their respective bases, we have $s = \sum_\tau s_\tau \varphi_\tau$ and $\overline{s} = \sum_{\overline{\tau}} \overline{s}_{\overline{\tau}} \overline{\varphi}_{\overline{\tau}}$, and computing the quantity $(s, \overline{\varphi}_{\overline{\tau}})$ yields

$$(s, \overline{\varphi}_{\overline{\tau}}) = \sum_{\tau \in \mathcal{T}_h} s_\tau \int_{\tau \cap \overline{\tau}} \varphi_\tau \overline{\varphi}_{\overline{\tau}} \, d\mathbf{x} \text{ for all } \overline{\tau} \in \overline{\mathcal{T}}_{\bar{h}}.$$

Introducing the matrix $\overline{G} = (g_{\overline{\tau}, \tau})$ where $g_{\overline{\tau}, \tau} = \int_{\tau \cap \overline{\tau}} \varphi_\tau \overline{\varphi}_{\overline{\tau}} \, d\mathbf{x}$, we can rewrite the integral moments in matrix-vector form as follows

$$(5.1) \qquad \overline{G}\boldsymbol{s} = \left(\sum_\tau g_{\overline{\tau}, \tau} s_\tau \right)_{\overline{\tau} \in \overline{\mathcal{T}}_{\bar{h}}} , \quad \boldsymbol{s} = (s_\tau)_{\tau \in \mathcal{T}_h}.$$

We are interested in the L^2-projection $s = \sum_\tau s_\tau \varphi_\tau$ of $\overline{s}$ onto Θ_h. Since $\overline{s} = \sum_{\overline{\tau}} \overline{s}_{\overline{\tau}} \overline{\varphi}_{\overline{\tau}}$, we have

$$(\overline{s}, \varphi_\tau) = \sum_{\overline{\tau} \in \overline{\mathcal{T}}_{\bar{h}}} \overline{s}_\tau \int_{\tau \cap \overline{\tau}} \varphi_\tau \overline{\varphi}_{\overline{\tau}} \, d\mathbf{x} \text{ for all } \overline{\tau} \in \overline{\mathcal{T}}_{\bar{h}},$$

which can be written in matrix-vector form as $W_h \boldsymbol{s} = \overline{G}^T \overline{\boldsymbol{s}}$ where $\overline{\boldsymbol{s}}$ is the vector of coefficients with entries $\overline{s}_{\overline{\tau}}$. Therefore, letting $G = \overline{G}^T$ we have

$$(5.2) \qquad \boldsymbol{s} = W_h^{-1} \overline{G}^T \overline{\boldsymbol{s}} = W_h^{-1} G \overline{\boldsymbol{s}} := \Pi_h \overline{\boldsymbol{s}},$$

where W_h is the (diagonal) mass matrix for the space Θ_h.

5.2. Implementation details of the L^2-projection operator. The Petrov-Galerkin assembly of the discrete L^2-projection Π_h requires computing the intersection between elements, and building a suitable set of quadrature points and weights from the intersection. Given two meshes $\mathcal{T}_h$ and $\overline{\mathcal{T}}_h$ we search for each pair of elements $\tau \in \mathcal{T}_h$ and $\overline{\tau} \in \overline{\mathcal{T}}_{\bar{h}}$ with intersection $I = \tau \cap \overline{\tau} \neq \emptyset$. We mesh the intersection I into a

simplicial complex I_h and map a suitable quadrature rule, such as standard Gaussian formulas [44], to each simplex $S \in I_h$. We transform the resulting quadrature points to the reference configuration of both elements τ and $\overline{\tau}$ and perform the assembly procedure.

One critical aspect for run time performance is intersection detection [45]. Of particular interest are linear time complexity algorithms such as spatial hashing [46] for quasi-uniform meshes, or advancing front algorithms [47] for meshes with varying size elements.

In large-scale parallel computations, meshes are generally arbitrarily distributed and no relationship between their elements is explicitly available. For determining such relationships based on spatial information, we consider parallel algorithms relying on space filling curves [48] and parallel tree searches [23]. We have implemented the algorithm in [23] by exploiting the software libraries MFEM [49], for handling the finite element representations, and MOONoLith [50], for handling the parallel intersection detection/computation and automatic load-balancing.

Here we summarize the overall parallel search approach which we implemented with MPI [51]. Our strategy exploits the implicit and self-affine structure of octrees for adaptively constructing a bounding volume hierarchy (BVH) fitting the volume of interest. While the octree is a global object, hence the volume described by the root cell $C_0 \supseteq D \cup \overline{D}$ is the same for all processes, and can be refined in the same way by any process without any communication, the BVH is constructed using local geometric information that needs to be exchanged for intersection testing. Similar to the octree, the bounding volumes associated with the BVH nodes are axis-aligned bounding-boxes (AABBs). However, instead of following the octree predefined subdivision pattern, the AABBs of the BVH fit the data more accurately and do not necessarily form a partition. For each octree cell C_n of node n, we have an associated bounding-box B_n^p which is part of the BVH constructed by process p. The extra BVH allows us to have tighter bounding volumes for the nodes at coarse levels of our hybrid hierarchy, hence allowing early pruning when performing tree-searches and dramatically improving the performance of the search. The goal of using this hybrid octree/BVH data-structure is to perform a cheap broad-phase intersection test without the need of exchanging mesh data.

Next we give a brief explanation of the several steps of our algorithm which are analyzed in terms of parallel performance in Section 7, Figures 4 and 7. These steps consists of *element bounding volumes generation*, *BVH comparison*, *load balancing*, *matching and rebalancing*, and *computation* of the L^2-projection operator.

In the *element bounding volumes generation* step, we compute the AABB for each element of the input meshes which we use for inserting the element in the octree/BVH data-structure.

In the *BVH comparison* step, we construct both the octree/BVH and we perform a search in the branches of the tree where there are potential intersections. In a potential intersection region containing $D \cap \overline{D}$ we adaptively refine the tree in an iterative fashion. At each iteration we refine the octree/BVH, and exchange the necessary information for constructing the search paths (or tree-traversals) consistently. Each pair of processes $\{p, q\}$ has dedicated search-paths which are updated/refined only when the required data (MPI-message) is available using asynchronous point-to-point communication. This data consists of the bounding-volumes B_n^p, B_n^q, which are tested for intersection, and the number of elements associated with each octree/BVH node n. If $B_n^p \cap B_n^q = \emptyset$ and if either p or q do not have elements associated with n, we stop the search for the sub-tree with root n for the pair of processes $\{p, q\}$.

From the BVH comparison we obtain a list L of tuples $\{n, p, q\}$, where n is a node of the octree/BVH and p is a process having elements intersecting with the bounding-box B_n^q of process q. Note that if $\{n, p, q\}$ exists then $\{n, q, p\}$ also exists and we consider them to be the same tuple. For any pair of processes p, q having an entry in L for node n we estimate the cost of performing the intersection test between the sets of elements associated with n by a cost function $\gamma_n(s_p, s_q) = s_p s_q$, where $s_k, k \in \{p, q\}$, is the size of the set of elements associated with n in the memory of process k.

The latter step allows us to perform the *load balancing* task. The load balancing is done by assigning the elements associated with each tuple $\{n, p, q\}$ in such a way that the work, according to the cost function $\gamma_n(s_p, s_q)$, is distributed as evenly as possible among processes. The load balancing algorithm exploits the ordering computed by linearization of the octree (i.e., Morton ordering) for splitting the work and grouping together nearby elements. Note that potential imbalances which might be caused by the output-sensitivity (i.e., the cost of the computation is influenced by the size of the output) of the problem due to both position and distribution of the elements are mitigated by the search procedure. This is only feasible because we delay the element-to-element intersection test to the latest possible moment. In fact, the next step which is the *matching and rebalancing* step, consists of communicating the necessary elements and determining the intersection pairs. Once we have the intersection pairs we re-balance once again, but this time at much finer granularity, to ensure an efficient *computation* step consisting on the actual element-to-element intersection computation and numerical quadrature for the assembly of the L^2-projection operator.

Our intersection-detection approach enables an efficient broad-phase intersection testing when the two (or more) finite element meshes are partially overlapping, which is the case for the problem presented in this paper. However, for the case where we have the prior knowledge that the two meshes are describing the same volume refining the tree before the construction of the search paths might provide slight performance improvements in tree-search phase of the intersection detection algorithm. For more details on parallel variational transfer we refer to [23].

6. Hierarchical SPDE Sampler. In this section we describe our proposed hierarchical SPDE sampling technique using domain embedding with non-matching meshes for MLMC simulations. We first describe the process of generating the sequences of coarser levels of $\overline{\mathcal{T}}_{\bar{h}}$, introducing the necessary finite element spaces and interlevel operators that will be used, followed by implementation details of mapping between non-matching meshes for coarse levels. Finally, the iterative solution strategy of the saddle-point problem is described for all levels.

6.1. Multilevel structure. We now describe the multilevel structure of the SPDE sampler using the structured grid of the regular domain $\overline{D}$. We assume that we have a nested sequence of meshes $\overline{\mathcal{T}}_\ell$ on the regular domain $\overline{D}$ for $\ell = 0, \ldots, L$ obtained by several steps of refinement of an initial coarse mesh $\overline{\mathcal{T}}_{h_L}$ with $\overline{\mathcal{T}}_0 = \overline{\mathcal{T}}_{\bar{h}}$. The corresponding finite element spaces $\overline{\mathbf{R}}_\ell, \overline{\Theta}_\ell$ are constructed for each coarse level to form a geometric hierarchy of standard Raviart–Thomas finite element spaces.

For $\ell = 0, \ldots, L$, we denote the saddle-point block matrices $\overline{\mathcal{A}}_\ell$ corresponding to the pair of finite element spaces $\overline{\mathbf{R}}_\ell, \overline{\Theta}_\ell$. The block interpolation operator for the

matrix $\overline{\mathcal{A}}_\ell$ is defined as

$$(6.1) \qquad \overline{\mathcal{P}} = \begin{bmatrix} P_{\mathbf{u}} & 0 \\ 0 & \overline{P}_\theta \end{bmatrix},$$

where $P_{\mathbf{u}}$ is the operator from the coarser space $\overline{\mathbf{R}}_{\ell+1}$ to the finer space $\overline{\mathbf{R}}_\ell$, and $\overline{P}_\theta$ is the piecewise constant operator from coarser space $\overline{\Theta}_{\ell+1}$ to the finer space $\overline{\Theta}_\ell$ for $\ell = 0, \ldots, L - 1$. These interpolation operators for the structured hierarchy of uniformly refined meshes are the canonical interpolation operators of geometric multigrid. Then, we write (4.7) at coarse level $\ell = 1, \ldots, L$ as

$$(6.2) \qquad \overline{\mathcal{A}}_\ell \overline{U}_\ell = \overline{F}_\ell,$$

where

$$\overline{\mathcal{A}}_\ell := \overline{\mathcal{P}}^T \overline{\mathcal{A}}_{\ell-1} \overline{\mathcal{P}}, \quad \overline{F}_\ell := \overline{\mathcal{P}}^T \overline{F}_{\ell-1}.$$

To conclude this section, we present the multilevel definition of the L^2-projection operator $\overline{G}_0 = \overline{G}$ presented in Section 5.1, see formula (5.1). By letting Π_0 denote L^2-projection operator on the fine mesh and $G_0 = \overline{G}_0^T$ denote the Petrov-Galerkin mass operator between the non-matching mesh at the fine grid level, we recursively define the L^2-projection operator between coarse meshes as

$$(6.3) \qquad \Pi_{\ell+1} = W_{\ell+1}^{-1} G_{\ell+1}, \quad G_{\ell+1} = P_\theta^T G_\ell \overline{P}_\theta,$$

where $W_{\ell+1}$ denotes the mass matrix in the space $\Theta_{\ell+1}$, and P_θ is the unstructured hierarchy's interpolation operator discussed in Section 3.1.

6.2. Hierarchical SPDE sampler with non-matching mesh embedding. We have shown that a realization of a Gaussian random field θ_h on $\mathcal{T}_h$ can be obtained by solving the linear system (4.7) for $\overline{\boldsymbol{\theta}}_{\bar{h}}$, then computing

$$(6.4) \qquad \boldsymbol{\theta}_h = \Pi_h \overline{\boldsymbol{\theta}}_{\bar{h}}.$$

From the linearity of the L^2-projection, it immediately follows that $\boldsymbol{\theta}_h \sim \mathcal{N}(\mathbf{0}, C_h)$, with $C_h = \Pi_h \overline{C}_{\bar{h}} \Pi_h^T$. This method proves to be scalable and efficient as it is able to leverage existing solvers and preconditioners for saddle-point problems with structured grids; however, the parametrization of θ is mesh-dependent. For MLMC, a realization of a Gaussian random field must be computed on a fine and coarse spatial resolution for the same random event ω. Thus, we consider generating $\theta_\ell(\omega)$ and $\theta_{\ell+1}(\omega)$ for the same ω.

As shown in [8], the Gaussian random field $\overline{\theta}_\ell(\omega)$ whose coefficient vector is given by

$$(6.5) \qquad \begin{bmatrix} \overline{\mathbf{u}}_\ell \\ \overline{\boldsymbol{\theta}}_\ell(\omega) \end{bmatrix} = \overline{\mathcal{A}}_\ell^{-1} \begin{bmatrix} 0 \\ -g \overline{W}_\ell^{1/2} \xi_\ell(\omega) \end{bmatrix}$$

admits the following two-level decomposition:

$$(6.6) \qquad \overline{\boldsymbol{\theta}}_\ell(\omega) = \overline{P}_\theta \overline{\boldsymbol{\theta}}_{\ell+1}(\omega) + \delta \overline{\boldsymbol{\theta}}_\ell(\omega),$$

where $\overline{\boldsymbol{\theta}}_{\ell+1}(\omega)$ is a coarse representation of a Gaussian random field from the same distribution on $\overline{\Theta}_{\ell+1}$, and

$$(6.7) \qquad \begin{bmatrix} \overline{\mathcal{A}}_\ell & \overline{\mathcal{A}}_\ell \overline{\mathcal{P}} \\ \overline{\mathcal{P}}^T \overline{\mathcal{A}}_\ell & 0 \end{bmatrix} \begin{bmatrix} \delta \overline{U}_\ell \\ \overline{U}_{\ell+1} \end{bmatrix} = \begin{bmatrix} \overline{\mathcal{F}}_\ell \\ 0 \end{bmatrix},$$

with the block expressions given by

$$\delta \overline{U}_\ell = \begin{bmatrix} \delta \overline{\mathbf{u}}_\ell \\ \delta \overline{\boldsymbol{\theta}}_\ell(\omega) \end{bmatrix}, \ \overline{U}_{\ell+1} = \begin{bmatrix} \overline{\mathbf{u}}_{\ell+1} \\ \overline{\boldsymbol{\theta}}_{\ell+1}(\omega) \end{bmatrix}, \ \text{and} \ \overline{\mathcal{F}}_\ell = \begin{bmatrix} 0 \\ -g\overline{W}_\ell^{1/2}\xi_\ell(\omega) \end{bmatrix}.$$

Given $\xi_\ell(\omega)$, we compute the realizations of the Gaussian field at levels ℓ and $\ell+1$ on the spaces Θ_ℓ and $\Theta_{\ell+1}$ by first computing $\overline{\boldsymbol{\theta}}_{\ell+1}$ by solving the saddle-point system (6.2) at level $\ell+1$ using the methodology described in Section 6.3. Then we compute $\overline{\boldsymbol{\theta}}_\ell$ by iteratively solving (6.2) at level ℓ with $\overline{\mathcal{P}U}_{\ell+1}$ as the initial guess. Finally, using the L^2-projection operators recursively defined by (6.3), we simultaneously transfer both $\overline{\boldsymbol{\theta}}_\ell$ and $\overline{\boldsymbol{\theta}}_{\ell+1}$ to the unstructured mesh hierarchy, and we write

$$\boldsymbol{\theta}_\ell = \Pi_\ell \overline{\boldsymbol{\theta}}_\ell, \quad \boldsymbol{\theta}_{\ell+1} = \Pi_{\ell+1} \overline{\boldsymbol{\theta}}_{\ell+1}.$$

6.3. SPDE sampler saddle-point problem linear solution. We now discuss our methodology for the solution of the saddle-point system (4.7) using a scalable solver for $H(\mathrm{div})$ problems. The hybridization solver that we employ reduces the original saddle-point system to a symmetric, positive definite system, which after appropriate diagonal rescaling (cf. [52]) is successfully solved by classical AMG solvers designed for H^1 equivalent problems. The hybridization approach is a classical technique used for solving saddle-point problems arising from discretizations of mixed systems posed in $H(\mathrm{div})$. More specifically, in our setting, we have a saddle-point matrix of the form

$$\begin{bmatrix} \overline{M} & \overline{B}^T \\ \overline{B} & -\overline{W} \end{bmatrix}.$$

Hybridization refers to decoupling the degrees of freedom associated with the interfaces between the elements of the mesh corresponding to the first, vector unknown $\overline{\mathbf{u}}$ (coming from the Raviart–Thomas space), and then imposing the difference of the decoupled quantities from both sides of the element interfaces to be zero posed as constraints using Lagrange multipliers. In this way, one ends up with an equivalent saddle-point system with one extra set of unknowns, namely the Lagrange multipliers $\boldsymbol{\lambda}$. The embedding system consists of the now decoupled (element-by-element) vector unknown $\widehat{\mathbf{u}}$, the original piecewise constant unknowns $\overline{\boldsymbol{\theta}}$ and the Lagrange multipliers $\boldsymbol{\lambda}$. The resulting matrix is symmetric with saddle-point form

$$\begin{bmatrix} \widehat{M} & \widehat{B}^T & \overline{C}^T \\ \widehat{B} & -\overline{W} & 0 \\ \overline{C} & 0 & 0 \end{bmatrix}.$$

Above, $\overline{C}$ is the matrix coming from the constraint of zero jumps of the decoupled unknowns $\widehat{\mathbf{u}}$ across element interfaces. The main property of the embedding matrix is that its two-by-two principal submatrix

$$\begin{bmatrix} \widehat{M} & \widehat{B}^T \\ \widehat{B} & -\overline{W} \end{bmatrix}$$

is block-diagonal with blocks corresponding to degrees of freedom within each element (which are decoupled from the other elements). Therefore, the reduced Schur-

14

complement matrix

$$\left[\overline{C},\, 0\right] \begin{bmatrix} \widehat{M} & \widehat{B}^T \\ \widehat{B} & -\overline{W} \end{bmatrix}^{-1} \left[\overline{C},\, 0\right]^T = \overline{C}\left(\widehat{M} + \widehat{B}^T \overline{W}^{-1} \widehat{B}\right)^{-1} \overline{C}^T,$$

is s.p.d.; it is explicitly available and provably equivalent to an H^1-discretization matrix. One problem (discussed and resolved in [52]) is that depending on the choice of basis in the Raviart–Thomas space, one may need to diagonally rescale the Schur-complement so that the constant coefficient vector corresponds to the constant function. The latter affects the successful use of classical AMG methods (which implicitly assume that the constant vector is in the near null-space of the underlined matrix).

In our experiments the resulting hybridization linear system is solved with the conjugate gradient method preconditioned with *hypre*'s highly scalable BoomerAMG solver [34].

7. Numerical Results. We now demonstrate the numerical performance and parallel scalability of the hierarchical SPDE with non-matching mesh embedding, and include standard results from MLMC computations using our proposed SPDE sampler for two different three-dimensional spatial geometries.
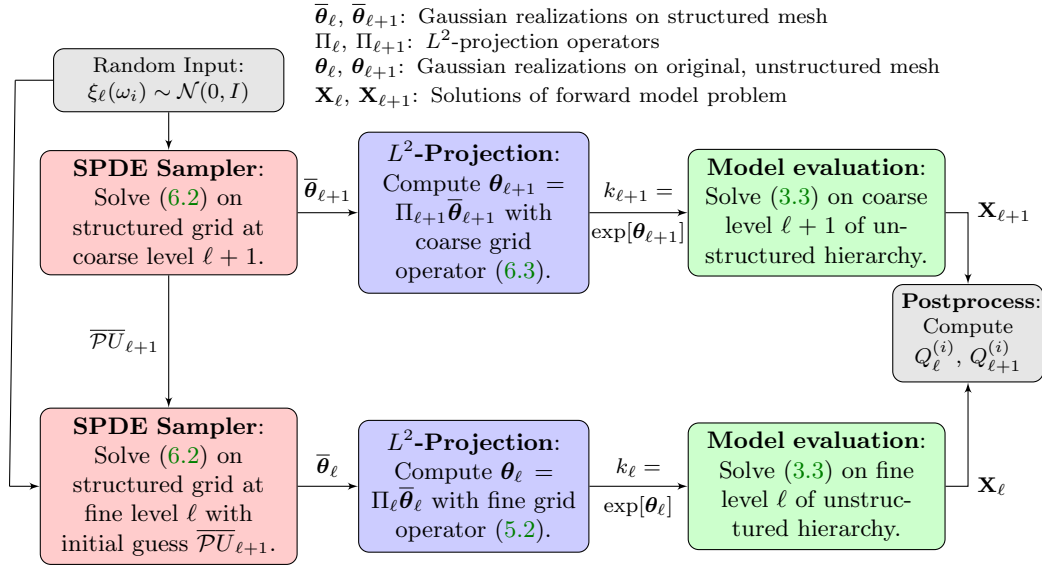
Fig. 1: Workflow to generate a sample, $Y_\ell^{(i)} = Q_\ell^{(i)} - Q_{\ell+1}^{(i)}$, for the MLMC estimator (2.4), where $Q_\ell^{(i)}$ is the QoI on the fine level, and $Q_{\ell+1}^{(i)}$ is the QoI on the coarse level with the same random sample $\omega^{(i)}$.

Figure 1 illustrates the workflow to generate a MLMC sample, $Y_\ell^{(i)} = Q_\ell^{(i)} - Q_{\ell+1}^{(i)}$, on a particular level ℓ for the estimator (2.4): First the random input coefficients are generated with our SPDE sampler using the non-matching mesh embedding on each level, then the forward model problem is solved on the original, unstructured grid.

7.1. Implementation details. We use the C++ finite element library MFEM [49] to assemble the discretized problems for the sampler and forward model problem. The hierarchy of discretizations, both structured and unstructured, are generated using the C++ library ParELAG [53], which uses a specialized element-based agglomeration technique to generate the algebraically constructed coarse spaces.

To formulate the right hand side of the SPDE sampler linear system (6.5), we must be able to draw a coefficient vector of suitable independent random numbers. In our numerical experiments, we use Tina's Random Number Generator Library [54] which is a pseudo-random number generator with dedicated support for parallel, distributed environments [55].

For the SPDE sampler, the saddle-point mixed linear system (6.2) is solved with the strategy described in Section 6.3 on each level, that is, hybridization where the reduced constrained system is solved with CG preconditioned with BoomerAMG [34]. The forward model discrete saddle-point system (3.3) is first assembled for each input realization, as discussed in detail in Section 3.1, see equations (3.4) and (3.5); then is solved with GMRES preconditioned with a block-LDU preconditioner, as described in Section 3.2, where the AMG preconditioner used to apply the action of the inverse of the approximate Schur-complement is recomputed for each input realization. The linear systems, both structured and unstructured, are iteratively solved with an absolute stopping criterion of 10^{-12} and a relative stopping criterion of 10^{-6}.

We now investigate the performance of the hierarchical sampler under weak scaling, i.e. when the number of mesh elements is proportional to the number of processes, and present results for MLMC simulations for two different three-dimensional domains. We consider a sequential, adaptive MLMC algorithm following [4] that estimates the discretization and sampling error from the computed samples and chooses the optimal values for N_ℓ "on the fly" during the MLMC simulation according to (2.6).

The numerical experiments were executed on *quartz*, a high performance cluster at Lawrence Livermore National Laboratory consisting of 2,688 nodes where each node has 128 GB of main memory and 36 cores operating at a clock rate of 2.1 GHz, for a total of 96768 cores. We use the full capacity of the nodes, i.e. 36 MPI processes per node.

7.2. Crooked pipe problem. We first consider a cylindrical "butterfly"-type grid, with highly stretched elements that are used to capture the boundary layer at the interface between two material subdomains. The domain D, a quarter cylinder with radius equal 2 and height equal 7, is embedded in the regular grid given by $\overline{D} = (0,3) \times (0,3) \times (0,8)$. Each mesh is uniformly refined several times to build the hierarchy of levels. Figure 2 shows the initial mesh for the crooked pipe problem and the enlarged, regular domain $\overline{D}$. The parameters of the random field are variance $\sigma^2 = 1$ and correlation length $\lambda = 0.3$. A sequence of computed Gaussian field realizations on different levels is shown in Figure 3.

We examine the performance of the SPDE sampler under weak scaling for the crooked pipe domain in Figure 4. The computational time to construct the SPDE sampler and generate 100 Gaussian realizations on the fine level with $5.1 \cdot 10^4$ stochastic degrees of freedom per process is examined in Figure 4a. In our approach the construction time of the L^2-projection operator takes about $16 - 18\%$ of the total computational time to generate 100 Gaussian realizations (Figure 4a). Weak scaling computational times to construct the L^2-projection operator with $1.1 \cdot 10^5$ input elements per process on the fine level are reported in Figure 4b for both the *search and*

(a) Crooked pipe problem

(b) Regular enlarged mesh embedding

(c) Slice view of non-matching mesh structure
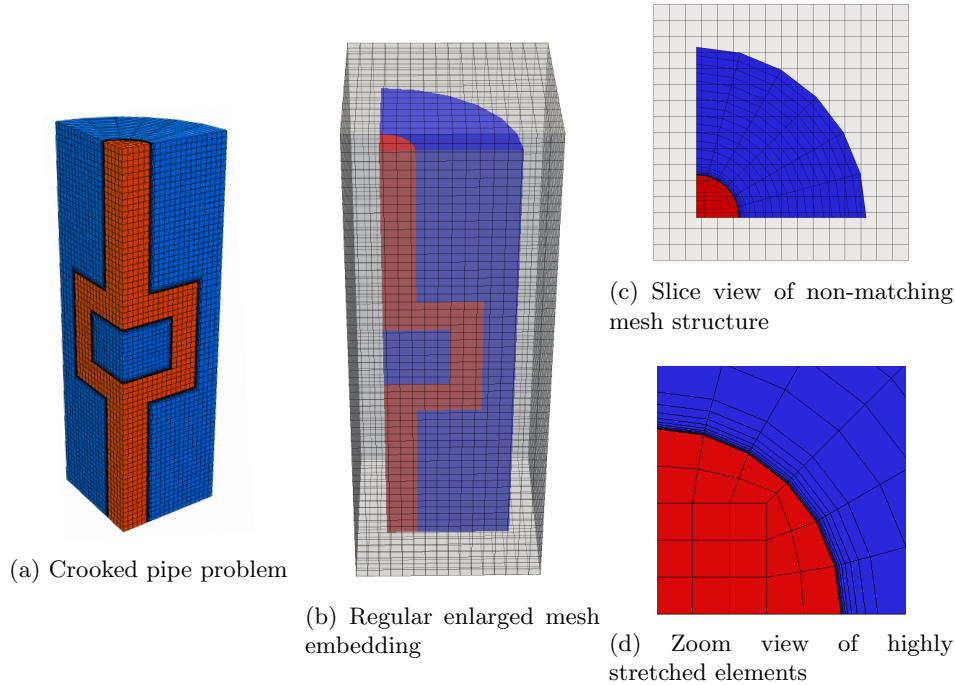
(d) Zoom view of highly stretched elements

Fig. 2: The initial crooked pipe mesh D, a quarter cylinder shape with radius equal to 2 and height equal to 7, featuring highly stretched elements that are used to capture the boundary layer at the interface between two material subdomains, with 14370 hexahedral elements and the larger, regular bounding box $\overline{D} = (0, 3) \times (0, 3) \times (0, 8)$ with 15360 hexahedral elements.

balancing and *computation* phase, and the detailed computational times are shown in Figure 4c where *search and balancing* includes all measurements except the computation. The timing labels are described in Section 5.2.

The *search and balancing* phase finds intersecting elements and redistributes elements to ensure load balancing of the computation. The search is a global process which requires communication and synchronization which leads to additional overhead when adding more processes. As described in Section 5.2, the search algorithm is based on the construction of an octree. The cost of this step can be tuned by the user by changing tree construction parameters such as maximum tree-depth and maximum number of elements per tree-node, however the computation has a lower bound computational time complexity $\Omega(n \log_8 n)$, where n is the number of input elements. From this lower bound we can expect that when increasing the size of the input by one order of magnitude we loose approximately 50% weak-scaling efficiency when searching for intersecting element pairs (Figure 4c). These limitations are represented in the measurements. With loss of generality the intersection detection could be further optimized for dealing with Cartesian grids where usually the (implicit) grid information is globally known [56]. In the *computation* phase we calculate polyhedral intersections and perform numerical quadrature. Here we also determine the exact size of the output which cannot be predicted accurately in advance, hence we

(a) Level $\ell = 0$ (b) Level $\ell = 1$ (c) Level $\ell = 2$ (d) Level $\ell = 3$
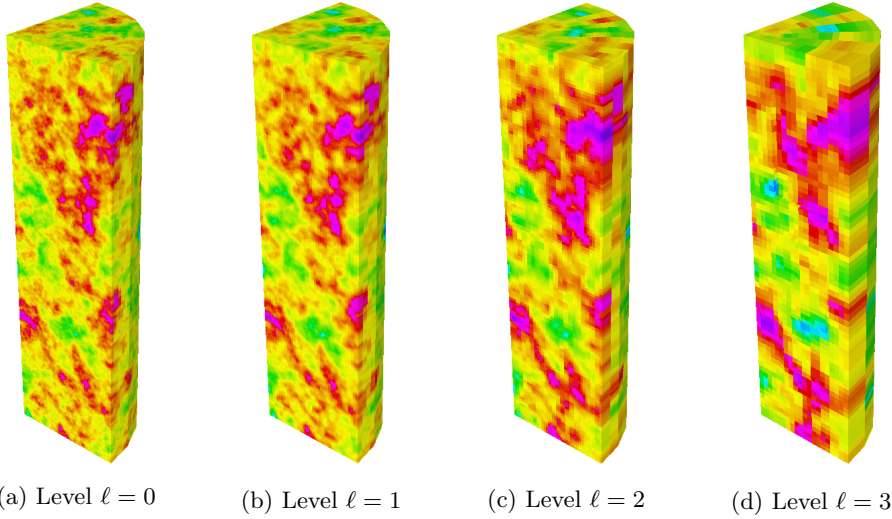
Fig. 3: A realization of the Gaussian random field on the crooked pipe domain obtained by using our hierarchical sampling technique for 4 levels with Matérn covariance with correlation length $\lambda = 0.3$.

encounter unavoidable slight computational imbalances.

Figure 5 shows the average time — for a number of MPI processes ranging from 144 to 9216 — to compute a realization on $\overline{D}$ and project the solution to the crooked pipe domain, D, with approximately $5.1 \cdot 10^4$ stochastic degrees of freedom per process on the fine level. We observe approximately 74% parallel efficiency for the fine level with 9216 processes to compute a realization using the sampling method with the scalable hybridization multigrid preconditioning strategy.

Now we consider a MLMC simulation with the forward model given by (3.1) with boundary conditions given by

$$\begin{cases} -p & = 1 \quad \text{on } \Gamma_{in}, \\ -p & = 0 \quad \text{on } \Gamma_{out}, \\ \mathbf{q} \cdot \mathbf{n} & = 0 \quad \text{on } \Gamma_s := \partial D \setminus (\Gamma_{in} \cup \Gamma_{out}), \end{cases}$$

where Γ_{in} is the boundary along the plane at $z = 0.5$ and Γ_{out} is the boundary along the plane at $z = 7.5$.

The random input coefficient is assumed to be log-normal with Matérn covariance (equivalent to an exponential covariance since $d = 3$) with $\sigma^2 = 1$ and correlation length $\lambda = 0.3$. The hierarchical SPDE sampler with mesh embedding is used to generate the input realizations. The quantity of interest is the expected value of the effective permeability, that is the flux through the "outflow" part of the boundary, defined as

$$(7.1) \qquad k_{eff}(\omega) = \frac{1}{|\Gamma_{out}|} \int_{\Gamma_{out}} \mathbf{q}(\cdot, \omega) \cdot \mathbf{n} \, dS.$$

In Figure 6, we present standard MLMC results for a 4-level method using 9216 processes with approximately $1.9 \cdot 10^9$ velocity and pressure degrees of freedom on

18

Processes	144	1152	921...
Construct Π_0	27.1485	29.7894	42.025...
Preconditioner Set-up	2.7156	2.8003	2.962...
Solve (4.7) for $\bar{\boldsymbol{\theta}}_0$	140.6940	157.1750	191.712...
Compute $\boldsymbol{\theta}_0 = \Pi_0\bar{\boldsymbol{\theta}}_0$	1.3203	1.2112	0.933...

(a) Computational time (secs) of generating 100 Gaussian realizations on the fine level using SPDE sampler.
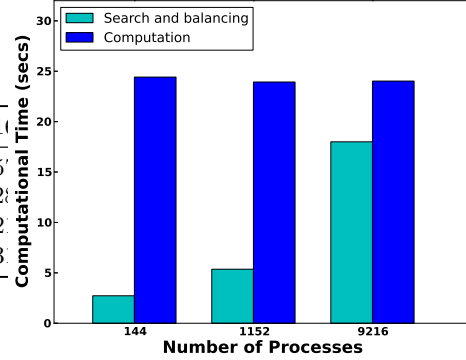
(b) Overview of the search and computation times for the assembly of the L^2-projection.

Processes	144	1152	9216
Element bounding volumes generation	0.1783	0.1788	0.1783
BVH comparison	0.4726	0.6303	2.5610
Load balancing	0.6702	1.2605	1.385
Matching and rebalancing	1.4066	3.7860	13.8728
Computation: intersection and quadrature	24.4207	23.9338	24.0251
Total	27.1485	29.7894	42.0257

(c) Detailed computational times for the assembly of the L^2-projection. Listed above the dashed-line are the different components of the *search and balancing* phase.

Fig. 4: The computational cost for the crooked pipe mesh of generating 100 Gaussian realizations on the fine level under weak scaling with approximately $5.1 \cdot 10^4$ stochastic degrees of freedom per process is shown in (a). The weak scalability of the L^2-projection operator assembly where the input is approximately $1.1 \cdot 10^5$ elements per process and the average number of intersections per process is $3.0 \cdot 10^5$ is demonstrated in (b) and (c). The computational time is divided between a *search and balancing* phase and a phase of *computation* of the transfer operator in (b) with the detailed timing results exhibited in (c).

the fine level and target MSE $\varepsilon^2 = 6.25 \cdot 10^{-6}$. Figure 6a displays the multilevel MC estimator, where the blue solid line represents the expectation at each level, $\mathbb{E}[Q_\ell]$, and the green dashed line represents the expectation of the correction, $\mathbb{E}[Q_\ell - Q_{\ell+1}]$. Figure 6b illustrates the multilevel variance reduction where the blue solid line shows the variance of the estimator for a particular level, whereas the green dashed line shows the variance of the correction for each level. This plot demonstrates the effectiveness of the MLMC method: as the number of unknowns (i.e. the spatial resolution) increases, the variance of the correction is reduced. The average sampling time to generate the required Gaussian field realizations and solve the forward model for each level is shown in Figure 6c. This plot indicates near optimal scaling of the MLMC method with the proposed hierarchical sampler. Figure 6d compares the predicted ε^2-cost of
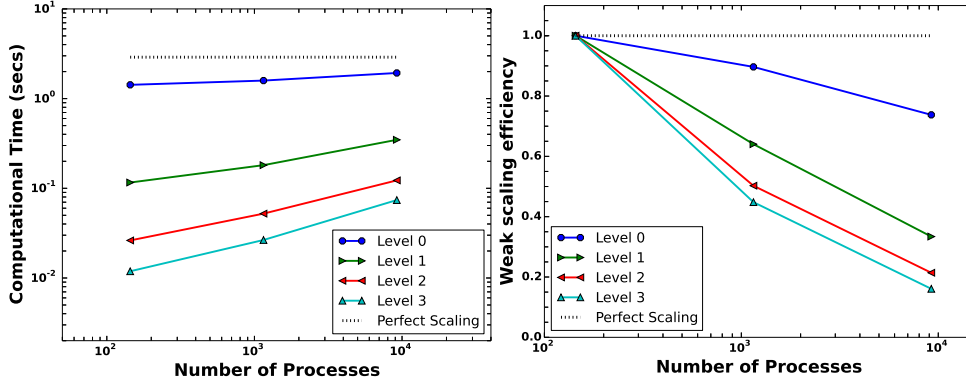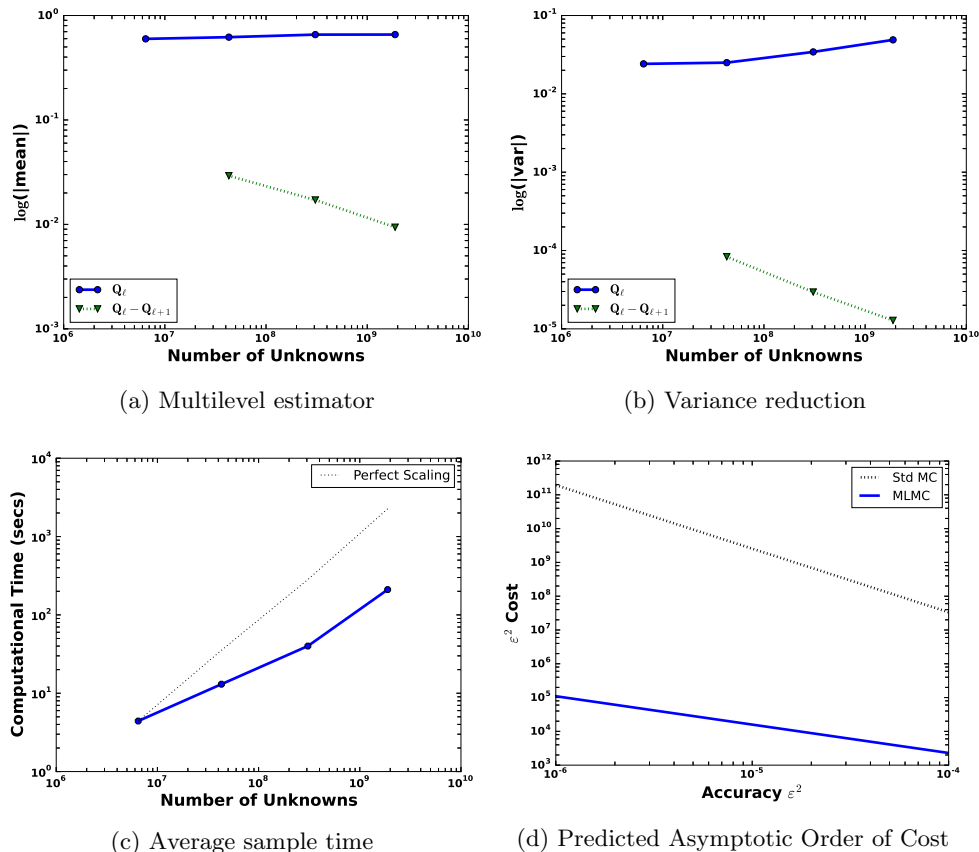
Fig. 5: Weak scalability of the linear solve time and L^2-projection operator applied for the hierarchical SPDE sampler on the crooked pipe domain where the size of the stochastic dimension per process, approximately $5.1 \cdot 10^4$ stochastic degrees of freedom on the fine level, is fixed. The size of the stochastic dimension of the finest level ranges from $7.4 \cdot 10^6$ to $4.7 \cdot 10^8$, and the number of MPI processes ranges from 144 to 9216. We observe approximately 74% parallel efficiency for the fine level with 9216 processes to compute a realization using the sampling method.

the standard MC and MLMC estimators using Theorem 2.3 from [5] with numerically observed constants estimated from Figures 6a-6c. The detailed computational time spent on each level is shown in Figure 6e, where the majority of the time is spent generating samples on the coarsest level.

Next we consider the performance of a MLMC simulation for the crooked pipe problem under weak scaling, where the number of velocity and pressure degrees of freedom per process is fixed. Table 1 displays the results of three MLMC simulations with increasing spatial resolution along with the processor count, while the desired MSE is decreasing. The tolerance for the sampling error is chosen to balance the estimated discretization error so more samples are necessary as a finer spatial resolution is used, yet the majority of the samples are computed on the coarsest level.

7.3. SPE10 problem. Next we consider the domain from Model 2 of the tenth SPE comparative solution project (SPE10) [57], a challenging benchmark for reservoir simulation codes. The domain is a 3D box with dimension $1200 \times 2220 \times 170$(ft) meshed with hexahedral elements. The mesh is embedded in a bounding box with dimension $1600 \times 2420 \times 240$(ft).

We first examine the performance of the SPDE sampler under weak scaling and assume the random field has $\sigma^2 = 1$ and correlation length $\lambda = 50$(ft). In Figure 7, we examine the set-up costs associated with the SPDE sampler and the computational time to generate 100 samples on the fine level with approximately $6.2 \cdot 10^4$ stochastic degrees of freedom per process. In our approach the construction time of the L^2-projection operator takes about $5 - 6\%$ of the total computational time to generate 100 Gaussian realizations (Figure 7a). Using the labels described in Section 5.2 for the computational components, the weak scaling of the construction of the L^2-projection operator is shown in Figures 7b and 7c, which displays a scaling behavior consistent with the results and discussion covered in Section 7.2 for the crooked pipe problem.

20

(a) Multilevel estimator

(b) Variance reduction

(c) Average sample time

(d) Predicted Asymptotic Order of Cost

Level	0 (fine)	1	2	3 (coarse)
Number of samples	42	99	234	7678
Realize input coefficients (SPDE sampler)	95.6791	46.5105	45.9743	567.5747
Assemble systems (3.3) on levels ℓ and $\ell+1$	315.2517	123.2833	20.1287	86.9110
Build AMG preconditioner for $\tilde{S}_\ell$ and $\tilde{S}_{\ell+1}$ in (3.6)	4.1919	2.5160	0.8775	10.3692
Solve (3.3) on levels ℓ and $\ell+1$	2516.1402	3557.3076	4172.4751	19903.6026
Total time	2931.2629	3729.6174	4239.4555	20568.4575

(e) Detailed computational times (secs) for each level of the MLMC simulation.

Fig. 6: MLMC results for crooked pipe problem when estimating the effective permeability, where the target MSE is $\varepsilon^2 = 6.25 \cdot 10^{-6}$ using 9216 processes with approximately $1.9 \cdot 10^9$ velocity and pressure degrees of freedom on the fine level. The expected value of the MC estimator of Q_ℓ and the correction are shown in (a) and the variance reduction of the multilevel method is shown in (b) where the variance of the multilevel correction term is significantly smaller than the variance of the MC estimator of Q_ℓ. In (c), the average sampling time to generate a MLMC sample $Y_\ell^{(i)} = Q_\ell^{(i)} - Q_{\ell+1}^{(i)}$ for each level versus the number of unknowns on level ℓ is plotted. Plot (d) compares the theoretical asymptotic order of cost to achieve a MSE of ε^2 for this problem formulation for the standard MC and MLMC estimators. The MLMC method leads to a significant improvement over the standard MC method. The time spent on each level of the MLMC hierarchy is shown in (e).

Table 1: Weak scaling of the crooked pipe problem for adaptive MLMC simulations where the number of degrees of freedom per process is kept approximately fixed with approximately $2.1 \cdot 10^5$ pressure/velocity degrees of freedom per process on the fine level. In each row, the number of MPI processes are listed along with the number of velocity and pressure degrees of freedom on the fine level ($\ell = 0$), the desired MSE, the total computational wall time to run the MLMC simulation, the number of samples computed on the fine level (N_0), and the total number of computed samples on all levels for a 4 level method.

Processes	DOF ($\ell = 0$)	Target ε^2	Wall Time (s)	N_0	Total Samples
144	$2.96 \cdot 10^7$	$1.00 \cdot 10^{-4}$	$2.93 \cdot 10^2$	10	952
1152	$2.36 \cdot 10^8$	$2.50 \cdot 10^{-5}$	$1.65 \cdot 10^3$	21	3634
9216	$1.88 \cdot 10^9$	$6.25 \cdot 10^{-6}$	$3.15 \cdot 10^4$	42	8053

Figure 8 demonstrates the linear solver and L^2-projector application performance of the sampler under weak scaling with approximately $6.2 \cdot 10^4$ stochastic degrees of freedom per process on the fine level where the number of MPI processes ranges from 36 to 2304. The average time to compute a realization using our sampling method exhibits 68% parallel efficiency for 2304 processes on the fine level.

We now consider incorporating data from the SPE10 benchmark into a MLMC simulation. The random permeability coefficient $k(\mathbf{x}, \omega)$ is modeled as log-normal random field with mean equal to the absolute permeability given by the SPE10 dataset, so that

$$\exp[\log[k_{SPE10}(\mathbf{x})] + \theta(\mathbf{x}, \omega)],$$

where $\theta(\mathbf{x}, \omega)$ has an exponential covariance with $\sigma^2 = 1$ and correlation length $\lambda = 50(\text{ft})$. The hierarchical SPDE sampler with non-matching mesh embedding is used to generate the realizations of the random field $\theta(\mathbf{x}, \omega)$. Figure 9 illustrates the permeability field of the SPE10 dataset $k_{SPE10}(\mathbf{x})$. The forward problem is given by (3.1) with boundary conditions

$$\begin{cases} -p & = 1 & \text{on } \Gamma_{in} = \{0\} \times (0, 2200) \times (0, 170), \\ -p & = 0 & \text{on } \Gamma_{out} = \{1200\} \times (0, 2200) \times (0, 170), \\ \mathbf{q} \cdot \mathbf{n} & = 0 & \text{on } \Gamma_s := \partial D \setminus (\Gamma_{in} \cup \Gamma_{out}). \end{cases}$$

The quantity of interest is the expected value of the Darcy pressure evaluated on the fine element around the point $\mathbf{x}^* = (600, 1100, 85)$. Next we demonstrate the performance of a 4-level MLMC simulation using 2304 processes with approximately $1.4 \cdot 10^8$ velocity and pressure degrees of freedom on the fine level in Figure 10. The target MSE is set to $\varepsilon^2 = 6.25 \cdot 10^{-6}$.

The MC estimator of the QOI and the correction term on each level and the variance of both quantities are displayed in Figures 10a and 10b, respectively. The blue solid line represents the standard MC estimator at each level ℓ, whereas the green dashed line represents the MC estimator of the correction term. The MC estimates demonstrate the expected behavior, confirming the benefits of the multilevel approach, where the variance of the correction term decreases as the spatial resolution increases. The average sampling time to generate the required Gaussian field realizations and solve the forward model at each level is shown in Figure 10c. This plot

Processes	36	288	2304
Construct Π_0	6.9641	7.2735	7.6082
Preconditioner Set-up	2.0416	2.1059	2.2118
Solve (4.7) for $\bar{\boldsymbol{\theta}}_0$	91.2868	102.9320	135.1250
Compute $\boldsymbol{\theta}_0 = \Pi_0\bar{\boldsymbol{\theta}}_0$	0.5786	0.3380	0.4868

(a) Computational time (secs) of computing 100 Gaussian realizations on the fine level using SPDE sampler.
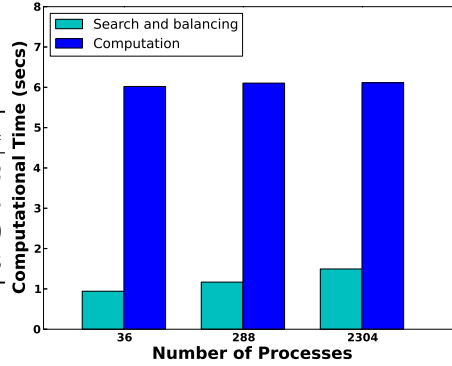
(b) Overview of the search and computation times for the assembly of the L^2-projection.

Processes	36	288	2304
Element bounding volumes generation	0.0702	0.0864	0.0873
BVH comparison	0.3738	0.3203	0.4937
Load balancing	0.3813	0.3704	0.3476
Matching and rebalancing	0.1174	0.3919	0.5664
Computation: intersection and quadrature	6.0213	6.1045	6.1132
Total	6.9641	7.2735	7.6082

(c) Detailed computational times for the assembly of the L^2-projection. Listed above the dashed-line are the different components of the *search and balancing* phase.

Fig. 7: The computational cost of generating 100 Gaussian realizations for $D = 1200 \times 2200 \times 170$ on the fine level under weak scaling with approximately $6.2 \cdot 10^4$ stochastic degrees of freedom per process is shown in (a). Weak scalability of the L^2-projection operator assembly with approximately $4.8 \cdot 10^4$ input elements per process where the average number of intersections per process is $1.5 \cdot 10^4$ is shown in (b) and (c). In (b), the computational time is divided between a *search and balancing* phase and a phase of *computation* of the transfer operator, where the detailed timing results are presented in (c).

demonstrates the desired scalability of the solution strategy for the forward problem and of the proposed hierarchical sampler with non-matching mesh embedding. The predicted ε^2-cost of the standard MC and MLMC estimators is shown in Figure 10d using Theorem 2.3 from [5] with numerically observed constants estimated from Figures 10a-10c. In Figure 10e, the computational time spent on each level illustrates the expected performance, where the majority of time is spent generating samples on the coarsest level. Next we consider the scalability of adaptive MLMC simulations for the SPE10 problem. Numerical results are presented in Table 2 for three different MLMC simulations where the spatial resolution is increasing, while the number of degrees of freedom per process remains approximately fixed. The desired MSE is chosen to balance the estimated discretization error with the sampling error, resulting in more
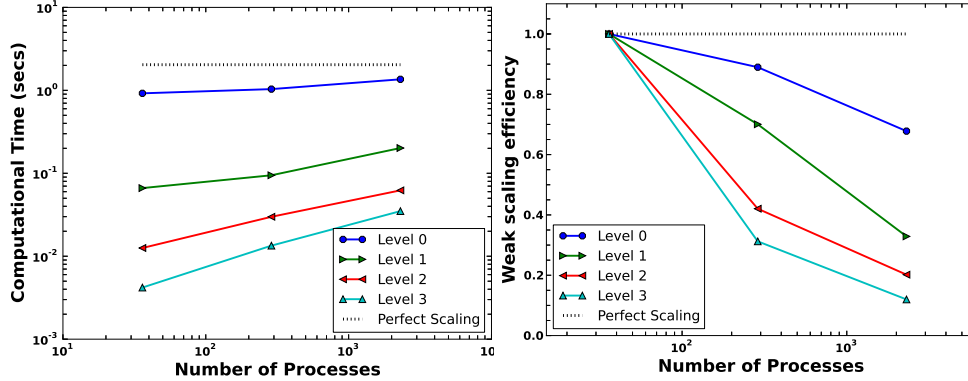
Fig. 8: Weak scalability of the hierarchical SPDE sampler on the domain with dimension $1200 \times 2220 \times 170$(ft) embedded in a box with dimension $1600 \times 2420 \times 240$(ft). The size of the stochastic dimension per process is fixed with approximately $3.3 \cdot 10^4$ stochastic degrees of freedom per process on the fine level. The size of the stochastic dimension of the finest level ranges from $1.2 \cdot 10^6$ to $7.5 \cdot 10^7$ and the number of MPI processes ranges from 36 to 2304. The average time to compute a realization using the sampling method exhibits 68% parallel efficiency for 2304 processes on the fine level.

(a) x/y-component

(b) z component
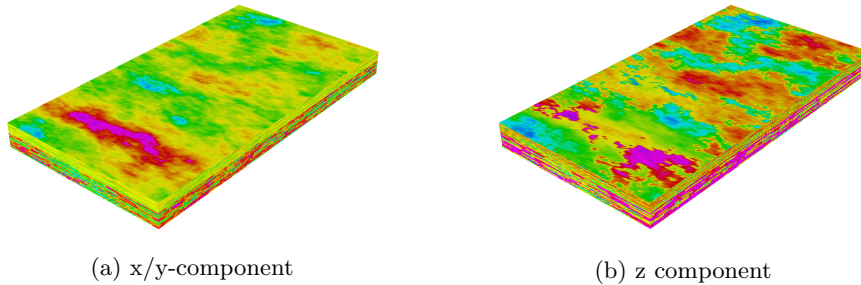
Fig. 9: Logarithmic plots of the absolute permeability coefficient from the SPE10 dataset which represents the mean of the log-normal random field used to model the random permeability field.

necessary samples for a finer spatial discretization while the majority of the samples are generated on the coarsest level.

7.4. Discussion. These results demonstrate that the parallel hierarchical SPDE sampler with non-matching domain embedding coupled with a scalable forward model solver allows for accurate large-scale MLMC simulations to be performed, which otherwise would not have been feasible. We have primarily focused on a novel, hierarchical sampling technique with non-matching mesh embedded for generating the necessary realizations of a Gaussian random fields. Our implementation is highly scalable with respect to the number of degree of freedom on the fine grid (74% parallel efficiency
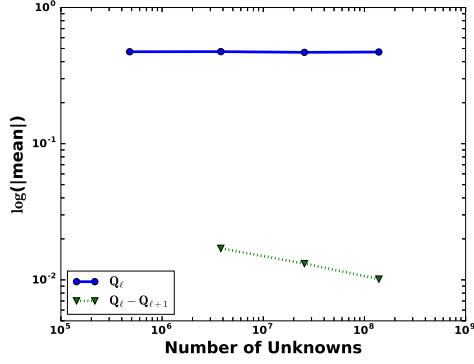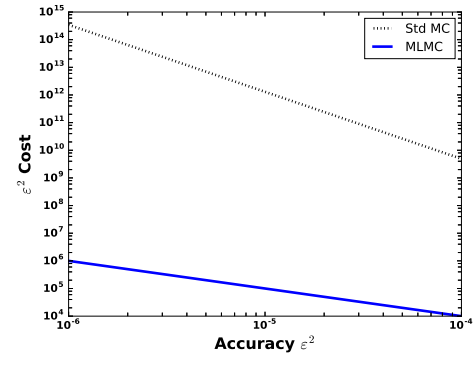
(a) Multilevel estimator
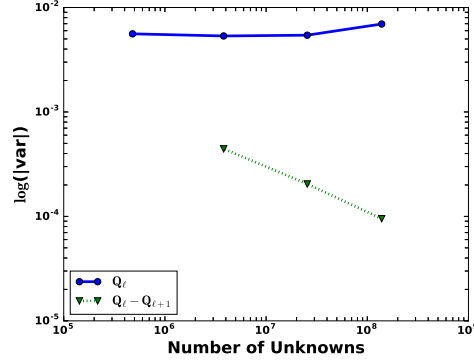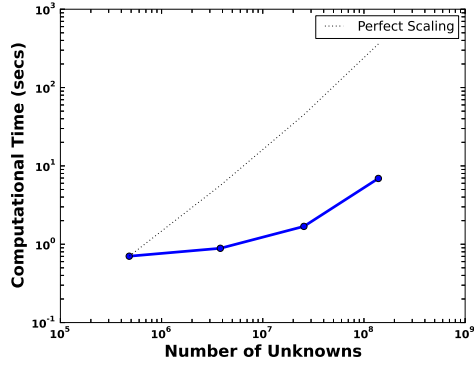
(b) Variance reduction

(c) Average sample time

(d) Predicted Asymptotic Order of Cost

Level	0 (fine)	1	2	3 (coarse)
Number of samples	148	419	766	4097
Realize input coefficients (SPDE sampler)	230.8140	110.5328	74.4681	143.3106
Assemble systems (3.3) on levels ℓ and $\ell+1$	144.0835	28.6440	7.4916	8.4634
Build AMG preconditioner for $\tilde{S}_\ell$ and $\tilde{S}_{\ell+1}$ in (3.6)	2.9663	1.1234	0.6655	1.3899
Solve (3.3) on levels ℓ and $\ell+1$	960.1115	1000.1379	1152.0609	2845.5386
Total time	1337.9754	1140.4381	1234.6861	2998.7025

(e) Detailed computational times (secs) for each level of the MLMC simulation.

Fig. 10: MLMC results for SPE10 problem where the target MSE is $\varepsilon^2 = 6.25 \cdot 10^{-6}$ using 2304 processes with approximately $1.4 \cdot 10^8$ velocity and pressure degrees of freedom on the fine level. The MC estimator at each level and the MC estimator of the correction is shown in (a) for each level, and the variance reduction of the multilevel method is demonstrated in (b), where the variance of the MC estimator and MC estimator of the correction term are plotted for each level. Plot (c) shows the average sampling time to generate the required Gaussian field realizations and solve the forward model for each level versus the number of unknowns. The theoretical asymptotic order of cost to achieve a MSE of ε^2 for this problem formulation comparing the standard MC and MLMC estimators is shown in Plot (d), where it is visible that the MLMC method leads to significant computational savings over the standard MC estimator. The time spend computing on each level is shown in (e) where the majority of time is spent on the coarse grid.

Table 2: Weak scaling of SPE10 problem for adaptive MLMC simulations with approximately $6.2 \cdot 10^4$ pressure/velocity degrees of freedom per process on the fine level. In each row, the number of MPI processes are listed along with the number of velocity and pressure degrees of freedom on the fine level ($\ell = 0$), the target MSE ε^2, the total computational wall time to run the MLMC simulation, the number of samples computed on the fine level (N_0), and the total number of computed samples on all levels for a 4 levels method.

Processes	DOF ($\ell = 0$)	Target ε^2	Wall Time (s)	N_0	Total Samples
36	$2.19 \cdot 10^6$	$1.00 \cdot 10^{-4}$	$3.09 \cdot 10^2$	12	641
288	$1.74 \cdot 10^7$	$2.50 \cdot 10^{-5}$	$1.26 \cdot 10^3$	46	2157
2304	$1.39 \cdot 10^8$	$6.25 \cdot 10^{-6}$	$6.45 \cdot 10^3$	148	5430

on 10 thousand processors). In addition, the overall parallel efficiency of the MLMC methods can be further improved by exploiting an additional layer of parallelism to generate multiple independent samples concurrently. In the current implementation, each sample is computed sequentially. We only exploit parallelism in the spatial dimension and, therefore, we use the same number of processors to solve the fine and coarser problems. This leads to an under utilization of computational resources on the coarser levels, where the problem size is too small with respect to the number of processors employed, and causes deterioration of performance in the linear solver phase. A significant improvement in the scalability of our methodology requires repartitioning the coarser problems on a subset of processes, so that multiple coarse samples can be computed in parallel and asynchronously by different subsets of processes. This approach has been investigated in [24], and can be applied directly applied also to our methods, modulo some implementation challenges and nuances all left for possible future studies.

8. Conclusions. The ability to efficiently generate samples of a Gaussian random field at different spatial resolutions is an essential component of large-scale sampling-based methods for forward propagation of uncertainty. We propose a hierarchical sampling method based on the solution of a reaction-diffusion stochastic PDE using a domain embedding technique with two non-matching meshes. The stochastic PDE is discretized and solved on a regular domain with a structured mesh, then transferred to the original, unstructured mesh of interest. The proposed sampling method allows for Gaussian random field realizations to be scalably generated for complex spatial domains, by leveraging efficient preconditioning techniques for the iterative solution of the discrete saddle-point problem arising from the discretization of the stochastic PDE on a regular domain. A hierarchical version of this process is explored, and numerical results demonstrate the scalability of the proposed method for generating realizations of a log-normal random field for large-scale simulations of flow in porous media. Additionally the sampling method is used in MLMC simulations of subsurface flow problems and numerical results are presented, which demonstrate the scalability of the hierarchical SPDE sampler with non-matching domain embedding for MLMC simulations of subsurface flow problems with over 470 million parameters in the stochastic dimension and 1.9 billion spatial unknowns.

REFERENCES

[1] Heinrich S. Multilevel Monte Carlo methods. *International Conference on Large-Scale Scientific Computing*, Springer, 2001; 58–67.

[2] Giles MB. Multilevel Monte Carlo path simulation. *Oper. Res.* 2008; **56**:607–617.

[3] Barth A, Schwab C, Zollinger N. Multi-level Monte Carlo finite element method for elliptic PDEs with stochastic coefficients. *Numer. Math.* 2011; **119**:123–161.

[4] Cliffe KA, Giles MB, Scheichl R, Teckentrup AL. Multilevel Monte Carlo methods and applications to elliptic PDEs with random coefficients. *Comput. Visual. Sci.* 2011; **14**:3–15.

[5] Teckentrup AL, Scheichl R, Giles MB, Ullmann E. Further analysis of multilevel Monte Carlo methods for elliptic PDEs with random coefficients. *Numer. Math.* 2013; **125**(3):569–600.

[6] Charrier J, Scheichl R, Teckentrup AL. Finite element error analysis of elliptic PDEs with random coefficients and its application to multilevel Monte Carlo methods. *SIAM J. Numer. Anal.* 2013; **51**(1):322–352, doi:10.1137/110853054. URL http://dx.doi.org/10.1137/110853054.

[7] Gittelson CJ, Könnö J, Schwab C, Stenberg R. The multi-level Monte Carlo finite element method for a stochastic Brinkman problem. *Numer. Math.* 2013; **125**(2):347–386, doi:10.1007/s00211-013-0537-5. URL http://dx.doi.org/10.1007/s00211-013-0537-5.

[8] Osborn S, Vassilevski PS, Villa U. A multilevel, hierarchical sampling technique for spatially correlated random fields. *SIAM J. Sci. Comput.* 2017; **39**(5):S543–S562, doi:10.1137/16M1082688.

[9] Lashuk I, Vassilevski PS. The construction of the coarse de Rham complexes with improved approximation properties. *Comput. Meth. in Appl. Math.* 2014; **14**(2):257–303, doi:10.1515/cmam-2014-0004.

[10] Lashuk IV, Vassilevski PS. Element agglomeration coarse Raviart–Thomas spaces with improved approximation properties. *Numer. Linear Alg. Appl.* 2012; **19**(2):414–426, doi:10.1002/nla.1819. URL http://dx.doi.org/10.1002/nla.1819.

[11] Pasciak JE, Vassilevski PS. Exact de Rham sequences of spaces defined on macro-elements in two and three spatial dimensions. *SIAM J. Sci. Comput.* 2008; **30**(5):2427–2446, doi:10.1137/070698178. URL http://dx.doi.org/10.1137/070698178.

[12] Delhomme J. Spatial variability and uncertainty in groundwater flow parameters: a geostatistical approach. *Water Resources Research* 1979; **15**(2):269–280.

[13] Gelhar LW. *Stochastic Subsurface Hydrology*. Prentice-Hall, 1993.

[14] Loéve M. Probability Theory, Vol. ii. *Graduate Texts in Mathematics* 1978; **46**:0–387.

[15] Saibaba AK, Lee J, Kitanidis PK. Randomized algorithms for generalized Hermitian eigenvalue problems with application to computing Karhunen-Loéve expansion. *Numer. Linear Alg. Appl.* 2016; **23**(2):314–339, doi:10.1002/nla.2026. URL http://dx.doi.org/10.1002/nla.2026, nla.2026.

[16] Dietrich CR, Newsam GN. Fast and exact simulation of stationary Gaussian processes through circulant embedding of the covariance matrix. *SIAM J. Sci. Comput.* 1997; **18**(4):1088–1107, doi:10.1137/S1064827592240555. URL http://dx.doi.org/10.1137/S1064827592240555.

[17] Park MH, Tretyakov M. A block circulant embedding method for simulation of stationary Gaussian random fields on block-regular grids. *International Journal for Uncertainty Quantification* 2015; **5**(6).

[18] Pekurovsky D. P3DFFT: A framework for parallel computations of Fourier transforms in three dimensions. *SIAM J. Sci. Comput.* 2012; **34**(4):C192–C209.

[19] Pippig M. PFFT: An extension of FFTW to massively parallel architectures. *SIAM J. Sci. Comput.* 2013; **35**(3):C213–C236.

[20] Whittle P. On stationary processes in the plane. *Biometrika* 1954; **41**:434–449.

[21] Whittle P. Stochastic processes in several dimensions. *B. Int. Statist. Inst.* 1963; **40**:974–994.

[22] Lindgren F, Rue H, Lindström J. An explicit link between Gaussian fields and Gaussian Markov random fields: the stochastic differential equation approach. *J. R. Stat. Soc. Series B* 2011; **73**:423–498.

[23] Krause R, Zulian P. A parallel approach to the variational transfer of discrete fields between arbitrarily distributed unstructured finite element meshes. *SIAM J. Sci. Comput.* 2016;

38(3):C307–C333.

[24] Drzisga D, Gmeiner B, Rüde U, Scheichl R, Wohlmuth BI. Scheduling massively parallel multi-grid for multilevel Monte Carlo methods. *SIAM J. Sci. Comput.* 2017; **39**(5):S873–S897.

[25] Haji-Ali AL, Nobile F, von Schwerin E, Tempone R. Optimization of mesh hierarchies in multilevel Monte Carlo samplers. *Stochastics and Partial Differential Equations Analysis and Computations* 2016; **4**(1):76–112, doi:10.1007/s40072-015-0049-7. URL http://dx.doi.org/10.1007/s40072-015-0049-7.

[26] Giles MB. Multilevel Monte Carlo methods. *Acta Numer.* 2015; **24**:259.

[27] Boffi D, Brezzi F, Fortin M. *Mixed Finite Element Methods and Applications*. Springer, 2013.

[28] Fortin M, Brezzi F. *Mixed and Hybrid Finite Element Methods*. Springer, 1991.

[29] Graham IG, Scheichl R, Ullmann E. Mixed finite element analysis of lognormal diffusion and multilevel Monte Carlo methods. *Stochastics and Partial Differential Equations Analysis and Computations* 2016; **4**(1):41–75.

[30] Kalchev D, Lee C, Villa U, Efendiev Y, Vassilevski P. Upscaling of mixed finite element discretization problems by the spectral AMGe method. *SIAM J. Sci. Comput.* 2016; **38**(5):A2912–A2933. URL http://dx.doi.org/10.1137/15M1036683.

[31] Christensen M, Villa U, Vassilevski PS. Multilevel techniques lead to accurate numerical upscaling and scalable robust solvers for reservoir simulation. *SPE Reservoir Simulation Symposium*, Society of Petroleum Engineers, 2015. URL https://www.onepetro.org/conference-paper/SPE-173257-MS, 23-25 February, Houston, Texas, USA, SPE-173257-MS.

[32] Christensen M, Villa U, Engsig-Karup A, Vassilevski PS. Numerical upscaling for incompressible flow in reservoir simulation: an element-based algebraic multigrid (AMGe) approach. *SIAM J. Sci. Comput.* 2017; **39**(1):B102–B137. URL https://doi.org/10.1137/140988991.

[33] Christensen M, Vassilevski PS, Villa U. Nonlinear multigrid solvers exploiting AMGe coarse spaces with approximation properties. *J. Comput. Math.* 2017; **available on-line**, doi: https://doi.org/10.1016/j.cam.2017.10.029.

[34] hypre: High performance preconditioners. https://computation.llnl.gov/projects/hypre-scalable-linear-solvers-multigrid-methods/software.

[35] Murphy MF, Golub GH, Wathen AJ. A note on preconditioning for indefinite linear systems. *SIAM J. Sci. Comput.* 2000; **21**(6):1969–1972, doi:10.1137/S1064827599355153.

[36] Chiles JP, Delfiner P. *Geostatistics: modeling spatial uncertainty*, vol. 497. John Wiley & Sons, 2009.

[37] Matérn B. *Spatial variation*, *Lecture Notes in Statistics*, vol. 36. Springer, 1986.

[38] Stuart AM. Inverse problems: A Bayesian perspective. *Acta Numer.* 2010; **19**:451–559, doi: doi:10.1017/S0962492910000061.

[39] Bui-Thanh T, Ghattas O, Martin J, Stadler G. A computational framework for infinite-dimensional Bayesian inverse problems Part I: The linearized case, with application to global seismic inversion. *SIAM J. Sci. Comput.* 2013; **35**(6):A2494–A2523, doi:10.1137/12089586X.

[40] Simpson D, Lindgren F, Rue H. In order to make spatial statistics computationally feasible, we need to forget about the covariance function. *Environmetrics* 2012; **23**(1):65–74.

[41] Lindgren F, Rue H. Bayesian spatial modelling with R-INLA. *Journal of Statistical Software* 2015; **63**(19).

[42] Daon Y, Stadler G. Mitigating the influence of the boundary on PDE-based covariance operators. *ArXiv e-prints* 2016; .

[43] Rusten T, Vassilevski PS, Winther R. Interior penalty preconditioners for mixed finite element approximations of elliptic problems. *Mathematics of Computation* 1996; **65**:447–466.

[44] Stroud A, Secrest D. *Gaussian Quadrature Formulaes*. Prentice Hall series in automatic computation, Prentice-Hall, 1966.

[45] Ericson C. *Real-Time Collision Detection (The Morgan Kaufmann Series in Interactive 3D Technology)*. Morgan Kaufmann Publishers Inc.: San Francisco, CA, USA, 2004.

[46] Lefebvre S, Hoppe H. Perfect spatial hashing. *ACM SIGGRAPH 2006 Papers*, SIGGRAPH '06, ACM: New York, NY, USA, 2006; 579–588, doi:10.1145/1179352.1141926. URL http://doi.acm.org/10.1145/1179352.1141926.

[47] Gander MJ, Japhet C. *An Algorithm for Non-Matching Grid Projections with Linear Complexity*. Springer Berlin Heidelberg: Berlin, Heidelberg, 2009; 185–192.

[48] Bader M. *Space-filling curves: an introduction with applications in scientific computing*, vol. 9. Springer Science & Business Media, 2012.

[49] MFEM: Modular finite element methods. http://mfem.org.

[50] MOONoLith: Multi-purpose object oriented numerics library. https://bitbucket.org/zulianp/par_moonolith.

[51] Forum MPI. MPI: A Message-Passing Interface Standard Version 3.0 Sep 2012. Chapter author for Collective Communication, Process Topologies, and One Sided Communications.

[52] Lee CS, Vassilevski PS. Parallel solver for H (div) problems using hybridization and AMG. *Domain Decomposition Methods in Science and Engineering XXIII* 2017; **116**:69.

[53] ParELAG: Element-agglomeration algebraic multigrid and upscaling library. http://github.com/LLNL/parelag.

[54] Tina's Random Number Generator Library. https://numbercrunch.de/trng/.

[55] Bauke H, Mertens S. Random numbers for large-scale distributed Monte Carlo simulations. *Physical Review E* 2007; **75**(6):066 701.

[56] Cavoretto R, Schneider T, Zulian P. OpenCL based parallel algorithm for RBF-PUM interpolation. *Journal of Scientific Computing* 2017; :1–23.

[57] Society of petroleum engineers. Tenth SPE comparative solution project. http://www.spe.org/web/scp.